ADVANCED SUSTAINABLE SYSTEMS
www.advsustainsys.com

Gas- and Liquid-Phase Catalysts for Solar-Driven Catalytic Ammonia Decomposition

*Zhuohao Yang, Xuechen Jing, Ruhan Liu, Zhipeng Cao, and Zongyou Yin**

As the transition toward a carbon-neutral hydrogen economy gains increasing attention, photocatalytic ammonia decomposition has received growing interest as a clean and scalable method for hydrogen production. This review critically summarizes recent progress in catalyst development, mechanistic understanding, and performance optimization for solar-driven ammonia decomposition. Photocatalytic systems are categorized by reaction phase (liquid phase and gas phase), and key strategies are discussed, including bandgap tuning, active site engineering, and cocatalyst integration. In addition, emerging approaches such as photothermal enhancement, single-atom catalysis, and machine learning-guided catalyst screening are examined. Current challenges, particularly catalyst deactivation, system-level integration, and scalability, are also highlighted, with a strong emphasis on the scalability of this method. Finally, perspectives are provided for future research aimed at bridging fundamental insights with practical applications. This work offers guidance for the rational design of efficient photocatalysts and contributes to the broader goal of sustainable hydrogen production via solar energy, providing reassurance about the practicality of this approach.

1. Introduction

At present, the world's major economies remain predominantly reliant on the consumption of fossil fuels.[1–5] In alignment with the United Nations Sustainable Development Goals (SDGs)—specifically SDG 7 (Affordable and Clean Energy) and SDG 13 (Climate Action)—a transition to clean energy is essential.[6–9] Hydrogen is an efficient and clean alternative energy source[10–12] with a high gravimetric energy density (119.7 MJ kg^{-1} of lower heating value at 25 °C and 1 bar, compared to gasoline's 44.79 MJ kg^{-1}); however, significant challenges remain in its storage and transportation.[13–15] Currently, it is stored either as compressed gas at 700 bar at room temperature or as liquid hydrogen at −252.9 °C and 1 bar.[16–18] To address these challenges, ammonia has been recognized as a promising alternative hydrogen source.

Ammonia is a widely produced commercial chemical, with a global production of ≈240 million metric tons in 2023.[19] Compared with other storage materials such as cyclohexane, ethanol, and liquefied petroleum gas, ammonia exhibits a high volumetric energy density (108 kg H_2 m^{-3} NH_3 at 20 °C and 8.6 bar) and gravimetric energy density (17.8 wt%), as well as ease of storage and transportation, making it an efficient hydrogen carrier.[20–23] Earlier studies on ammonia decomposition were generally conducted under high-temperature conditions. One of the earliest studies on ammonia decomposition was conducted in 1904 by Perman and Atkinson.[24] In recent years, as research has advanced, ammonia decomposition has been extensively investigated across various approaches, including thermal catalysis, electrocatalysis, plasma catalysis, and photocatalysis. Among these, thermal catalysis has received the most attention, owing to its relatively high performance and the availability of diverse catalytic systems. However, despite its industrial maturity, thermal catalysis still suffers from inherent limitations, such as the requirement for high operating temperatures (600–850 °C), reduced energy efficiency due to partial NH_3 combustion, and the complexity of the overall process.[25] These limitations underscore the urgent need to explore alternative strategies, among which solar-driven photocatalysis has emerged as a particularly promising direction.

Solar energy is the most abundant renewable resource available on Earth. Its predictable availability and broad spectral coverage make it especially attractive for photocatalytic applications.[26,27] Photocatalysis has attracted significant research interest since Fujishima and Honda reported photoelectrochemical (PEC) water splitting using titanium dioxide (TiO_2) as a photoanode in 1972.[28] From a thermodynamic perspective, the decomposition of ammonia, whether in the gaseous or liquid phase, is not particularly vigorous[29] (Equations (1) and (2)). Consequently, the relatively mild thermodynamic barriers, combined with ongoing improvements in semiconductor photocatalysts and solar energy utilization, strongly suggest that photocatalytic ammonia decomposition is feasible. Compared with thermal catalysis, photocatalysis directly harnesses abundant solar

Z. Yang, X. Jing, R. Liu, Z. Cao, Z. Yin
Research School of Chemistry
The Australian National University
Canberra, Australian Capital Territory 2601, Australia
E-mail: zongyou.yin@anu.edu.au

The ORCID identification number(s) for the author(s) of this article can be found under https://doi.org/10.1002/adsu.202500855

DOI: 10.1002/adsu.202500855

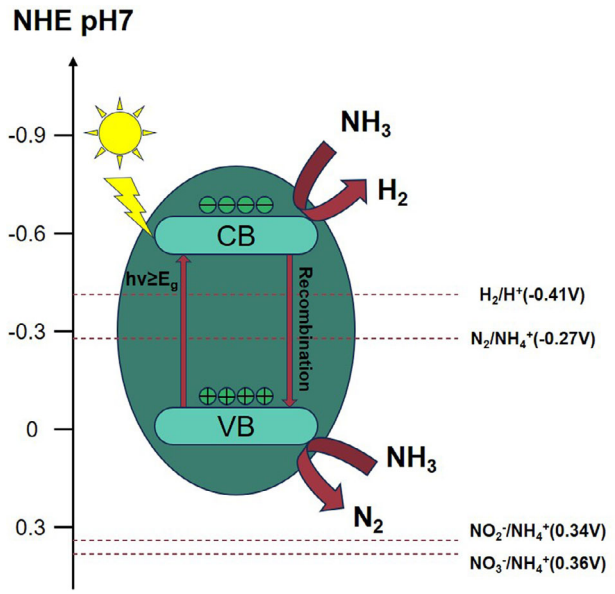

Figure 1. Photocatalytic ammonia decomposition potential.

energy, reducing reliance on fossil fuels, lowering overall energy input, and offering greater sustainability. In addition, redox reactions driven by photogenerated charge carriers enable higher energy efficiency, and the relatively mild reaction conditions confer better scalability and adaptability for practical applications.

$$2/3NH_3\ (g) \rightarrow H_2\ (g) + 1/3N_2\ (g)\ \Delta G^\circ = +11\ \text{kJ mol}^{-1} \quad (1)$$

$$2/3NH_3\ (aq) \rightarrow H_2\ (g) + 1/3N_2\ (g)\ \Delta G^\circ = +18\ \text{kJ mol}^{-1} \quad (2)$$

The photocatalytic decomposition of ammonia to produce hydrogen proceeds as follows: the photocatalyst is excited to generate photoinduced electron–hole pairs when the energy of the incident light is greater than the bandgap energy of the photocatalyst. Under these conditions, the photoinduced holes (h^+) in the valence band (VB) can oxidize ammonia molecules to N_2 and hydrogen ions (H^+), while the photogenerated electrons (e^-) in the conduction band (CB) subsequently reduce the H^+ to molecular H_2 (Equations (3)–(5))

$$\text{Photocatalyst} \rightarrow h^+ + e^- \quad (3)$$

$$2NH_3 + 6h^+ \rightarrow N_2 + 6H^+ \quad (4)$$

$$6H^+ + 6e^- \rightarrow 3H_2 \quad (5)$$

The potential diagram for photocatalytic ammonia decomposition is illustrated in **Figure 1**.[30] For the reduction of ammonia to proceed, its reduction potential must be higher than the CB of the semiconductor, while its oxidation potential must be lower than the VB. Currently, ammonia decomposition predominantly takes place under liquid-phase conditions. A range of photocatalysts has been explored for aqueous ammonia decomposition, including those based on common semiconductor materials such as TiO_2 and zinc oxide (ZnO), as well as catalysts incorporating Ru, an extensively studied metal in the thermal decomposition of ammonia. Although liquid-phase systems offer certain advantages in operational simplicity, the limited contact between ammonia molecules and the catalyst surface in aqueous environments, combined with the similar redox potentials of competing nitrogen species, often leads to the formation of undesired byproducts such as NO_2^- and NO_3^-. Through bandgap engineering, product selectivity can be partially controlled by aligning the valence-band potential more precisely with NH_3 oxidation, thereby suppressing side reactions. In addition, most gas-phase photocatalytic systems inherently avoid these issues, as water-derived •OH pathways are suppressed, reducing the formation of nitrate and nitrite byproducts.

Previous work, such as that by Zhang et al.,[31] primarily focused on ammonia degradation rather than achieving stoichiometric hydrogen generation. Although both processes involve catalytic transformation of NH_3, they differ fundamentally in reaction objectives, products, and operating conditions (**Table 1**).

Currently, research on photocatalytic ammonia decomposition receives limited attention and remains weakly linked to industrial applications. This review aims to address these gaps by systematically examining catalysts for both liquid- and gas-phase reactions, highlighting strategies in materials design, mechanistic interpretation, performance optimization, and linking them to the upstream and downstream segments of the ammonia–hydrogen value chain. It further outlines key challenges and future research directions toward scalable, solar-driven ammonia decomposition for practical clean hydrogen production, thereby advancing SDG 7 (Affordable and Clean Energy) and contributing to SDG 13 (Climate Action).

2. Photocatalysts for Hydrogen Production from Liquid-Phase Ammonia Decomposition

To provide a comprehensive overview of recent progress in photocatalytic hydrogen production from liquid-phase ammonia decomposition, **Table 2** summarizes recent advances and performance of these photocatalysts.

2.1. TiO_2-Based Photocatalysts

TiO_2 is widely regarded as a benchmark photocatalyst for hydrogen production from liquid-phase ammonia, owing to its chemical stability, low toxicity, and cost-effectiveness.[43–45] However, its practical performance is often limited by the rapid recombination of photogenerated charge carriers and a wide bandgap of ≈3.2 eV.[46,47] Various strategies have been explored to overcome these issues, including elemental doping and cocatalyst loading, to enhance charge separation and extend light absorption.

2.1.1. Monometallic TiO_2 Photocatalysts

TiO_2 typically crystallizes in three polymorphs: anatase, rutile, and brookite, each exhibiting distinct electronic structures and photocatalytic behavior. The crystalline phase and the choice of metal cocatalyst significantly influence hydrogen production efficiency. Kominami et al. synthesized TiO_2 powders using the HyCOM method from commercial P25 TiO_2.[32] Pt was loaded onto

Table 1. Comparison of ammonia degradation and ammonia decomposition.

	Ammonia degradation	Ammonia decomposition
Primary goal	Remove NH_3 as a pollutant from water	Convert NH_3 into H_2 (and N_2) as an energy carrier
Main products	NO_2^-, NO_3^-, N_2	H_2 (stoichiometric) + N_2
Reaction phase	Mostly liquid phase	Liquid phase or gas phase
Performance metrics	NH_3 removal efficiency (%)	H_2 production rate (μmol g^{-1} h^{-1})
Mechanistic focus	Hydroxyl radical (•OH) attacks oxidation	N_2H_4 dehydrogenation, N—N recombination
Energy relevance	Environmental remediation	Renewable energy generation

both uncalcined and variously calcined HyCOM-derived TiO_2 samples under identical reaction conditions, by adjusting the calcination parameters of the anatase-phase HyCOM TiO_2 to investigate the influence of the physical properties of TiO_2 on photocatalytic performance. The results revealed a linear correlation between the photocatalytic activity of HyCOM-derived TiO_2 and its specific surface area (**Figure** 2a), highlighting that surface area is a key factor governing hydrogen evolution from NH_3 in aqueous suspensions. Moreover, the rutile-phase samples loaded with Pt exhibited negligible photocatalytic activity, which Kominami et al. attributed to the intrinsically lower CB level of rutile, insufficient to facilitate H_2 generation.

In addition, Utsunomiya et al. conducted a further study comparing the photocatalytic activity of TiO_2 loaded with various transition metals for NH_3 decomposition under identical conditions.[33] The results showed that TiO_2 catalysts loaded with different transition metals—except for Ni—exhibited activity comparable to bare TiO_2, whereas the incorporation of Ni significantly enhanced the photocatalytic performance (Figure 2b). No formation of H_2 or N_2 was observed in the dark. Both H_2 and N_2 were generated upon UV irradiation, and their yields increased linearly with reaction time (Figure 2c). The molar ratio of H_2 to N_2 was 1:3, indicating that the products were formed stoichiometrically through the photocatalytic decomposition of NH_3.

Table 2. Photocatalysts for hydrogen production from liquid-phase ammonia decomposition.

Catalyst	Synthesis method	Initial concentration	Catalyst dosage	Light source	Temperature	H_2 production rate [μmol g^{-1} h^{-1}]	Stability	Refs.
Pt/TiO_2	Photodeposition	5 mL 0.1 mol L^{-1}	50 mg	400 W high-pressure mercury arc	298 K	450	/	[32]
$Ni(0.5\ wt\%)/TiO_2$	Impregnation	5 mL, 0.59 mol L^{-1}	20 mg	500 W Xe lamp	298 K	43.9	/	[33]
$Pd(0.3\ wt\%)/TiO_2$	Impregnation	30 mL 19.1 g L^{-1}	50 mg	Irradiation chamber	298 K	806.67	/	[34]
$Ce(1.2\ wt\%)/TiO_2$	Sol-gel process	100 mL, 0.8274 g L^{-1} (NH_4OH)	100 mg	8 W Hg pen-ray lamp	298 K	106	/	[35]
$Pt(0.1\ wt\%)/TiO_2$	Photodeposition	2 ml 15 mol L^{-1}	200 mg	300 W Xe lamp	308 K	560	/	[36]
$Pt_{0.9}Au_{0.1}/TiO_2$ (metal loadings 0.1 mol%)	Impregnation	100 ml 0.4 wt%	100 mg	2 kW Xe lamp	298 K	285.67	/	[37]
$Pt(0.5\ wt\%)$-Fe $(1.0\ wt\%)/TiO_2$	Solid-state reaction	5 mL, 0.59 mol L^{-1}	40 mg	500 W Xe lamp	298 K	5.8	/	[38]
rGO/TiO_2 NWs	Modified Hummers method	100 ml 0.883 g L^{-1}	5 mg	8 W 254 nm UV irradiation	298 K	208.33	/	[39]
ZnO	Thermal annealing	100 ml 0.8274 g L^{-1}	100 mg	8 W Hg pen-ray lamp	298 K	10.3	/	[29]
$Ru(0.7\ wt\%)/ZnS$	Photodeposition	150 ml 20 mmol L^{-1}	150 mg	300 W Xe lamp	298 K	5.13	/	[40]
$Ru(0.5\ wt\%)$ doped 2D α-Fe_2O_3	Impregnation	10 ml 28 wt%	2 mg	LED	298 K	156.25	120 h	[41]
Ru NPs/GaN NWs/Si	Photodeposition	1 mL 28 wt%	0.18 mg (0.36 mg cm^{-2})	300 W Xe lamp	743 K	1.1×10^7 (3.98 mmol cm^{-2} h^{-1})	400 h	[42]

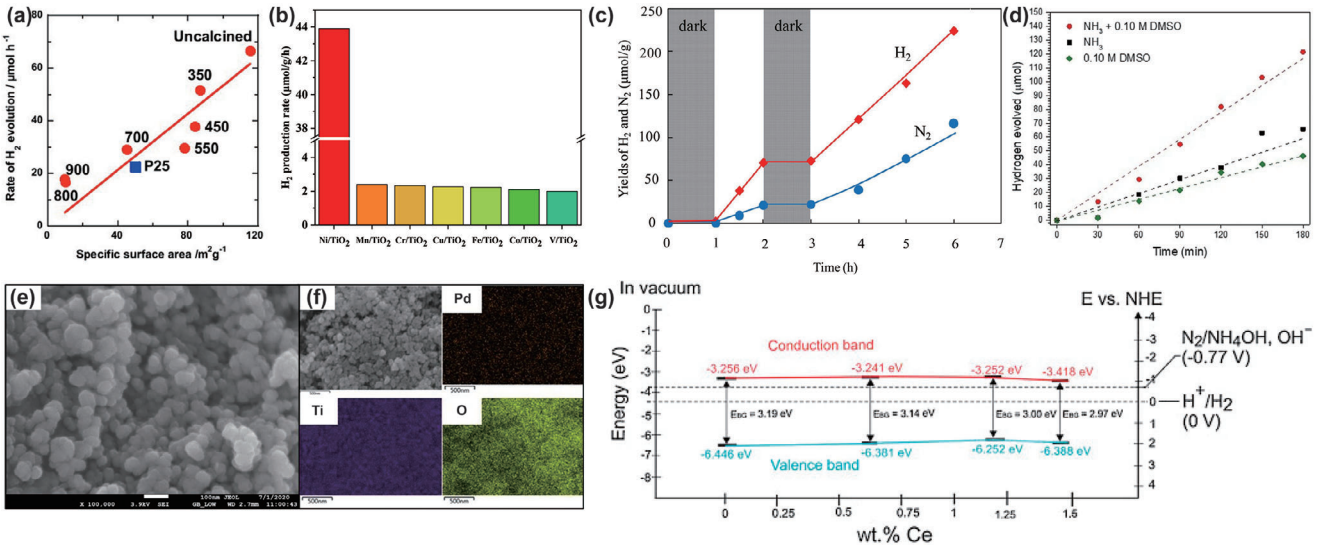

Figure 2. a) Effect of TiO_2 surface area (HyCOM and P25) on H_2 production from NH_3, reproduced with permission.[32] Copyright 2012, Elsevier. b) H_2 evolution using TiO_2 loaded with different transition metals. c) H_2 and N_2 yields over Ni/TiO_2 under light and dark cycles, reproduced with permission.[33] Copyright 2017, Elsevier. d) H_2 generation in NH_3, DMSO, and NH_3 + DMSO systems. e) FESEM image of 0.3 wt% Pd/TiO_2. f) EDX mapping of Pd, Ti, and O in 0.3 wt% Pd/TiO_2, reproduced with permission.[34] Copyright 2022, Springer Nature. g) Band structure changes with Ce doping, reproduced with permission.[35] Copyright 2015, Elsevier.

Using electron spin resonance (ESR) to monitor the formation of reaction intermediates during NH_3 decomposition, the authors proposed three reaction pathways (**Figure 3**). In Route 1, NH_3 radicals are formed by abstracting one hydrogen atom from each of two NH_2 radicals. Route 2 involves coupling adjacent NH_2 radicals to form NH_2—NH_2, while an alternative route, Route 2′, proceeds via the formation of H_2N—NH_3, which can also convert into NH_2—NH_2. Since Route 2 has a significantly lower activation energy than Route 1, it is considered energetically more favorable. The subsequent transformation of NH_2—NH_2 into N_2 and H_2 may proceed via either Route 2 (NH_2 radical coupling) or Route 2′ (interaction between NH_2 and gaseous NH_3). Given that the activation barriers of Route 2 and 2′ are comparable, it is likely that NH_3 decomposition proceeds through both routes, ultimately yielding NH_2—NH_2 as a key intermediate.

In another study, Abdul Razak et al. investigated the performance of Pd-loaded and metal-doped TiO_2 catalysts.[34] Through comparative experiments using Pd/TiO_2 in an NH_3 solution containing 0.1 M DMSO (Figure 2d), they found that hydrogen generation from NH_3 originated from the interaction between N atoms and the Pd surface, facilitated by photoexcited electrons, which promoted N—H bond cleavage. The Pd/TiO_2 catalyst, prepared via incipient wetness impregnation, exhibited a high dispersion of Pd species across the TiO_2 surface (Figure 2e,f). The addition of DMSO served as an •OH scavenger, suppressing further oxidation of H+ by •OH radicals and thereby enhancing hydrogen production. As a result, a hydrogen evolution rate as high as 806.67 μmol g^{-1} h^{-1} was achieved.

In addition to controlling the type of loaded metal and introducing radical scavengers, tuning the metal loading also holds promise for enhancing hydrogen evolution performance. Reli et al. were the first to investigate the photocatalytic decomposition of NH_3 over Ce-loaded TiO_2 (0.6, 1.2, and 1.4 wt%). Incorporating cerium led to an increase in the specific surface area of the catalyst and a reduction in bandgap energy. For the 0.6 wt% Ce/TiO_2 sample, the shifts in the conduction and VB edges were minimal compared to pristine TiO_2, as the differences in work function and absorption edge between TiO_2 and 0.6 wt% Ce/TiO_2 were negligible. Further increasing the Ce content to 1.2 wt% resulted in a slight upward shift of the CB by 15 meV and a more substantial upward shift of the VB by 129 meV. However, when the Ce content was raised to 1.4 wt%, the CB and VB positions decreased significantly by 229 and 136 meV, respectively (Figure 2g). A higher CB edge is more effective in facilitating the conversion of N_2/NH_4OH, thereby making the 1.2 wt% Ce/TiO_2 catalyst the most favorable for photocatalytic NH_3 decomposition. Experimental results well supported these theoretical findings. The 1.2 wt% Ce/TiO_2 catalyst exhibited the highest hydrogen evolution rate, reaching 106 μmol g^{-1} h^{-1}.

2.1.2. Bimetallic TiO_2 Photocatalysts

The synergistic effect of bimetallic cocatalysts on TiO_2 has been demonstrated to enhance the photocatalytic activity for NH_3 decomposition significantly. Pt-Au bimetallic alloy nanoparticles (NPs) supported on TiO_2 ($Pt_{1-x}Au_x/TiO_2$) have been investigated for liquid-phase NH_3 decomposition.[37]

Considering the band structure, the Schottky barrier (φ_B) at the metal/TiO_2 interface restricts the mobility of carrier transfer during photoactivation. However, back electron transfer in the low φ_B system suggests that a considerable energy barrier benefits charge separation. Therefore, the bimetallic strategy identifies a balance point in constructing photocatalysts (**Figure 4a**).[48] Among metals, Pt has the highest work function of 5.65 eV, which leads to a high Schottky barrier when deposited on TiO_2.[49] Consequently, Pt/TiO_2 catalysts may exhibit limited electron transfer due to this energy barrier. It is generally recognized that alloying

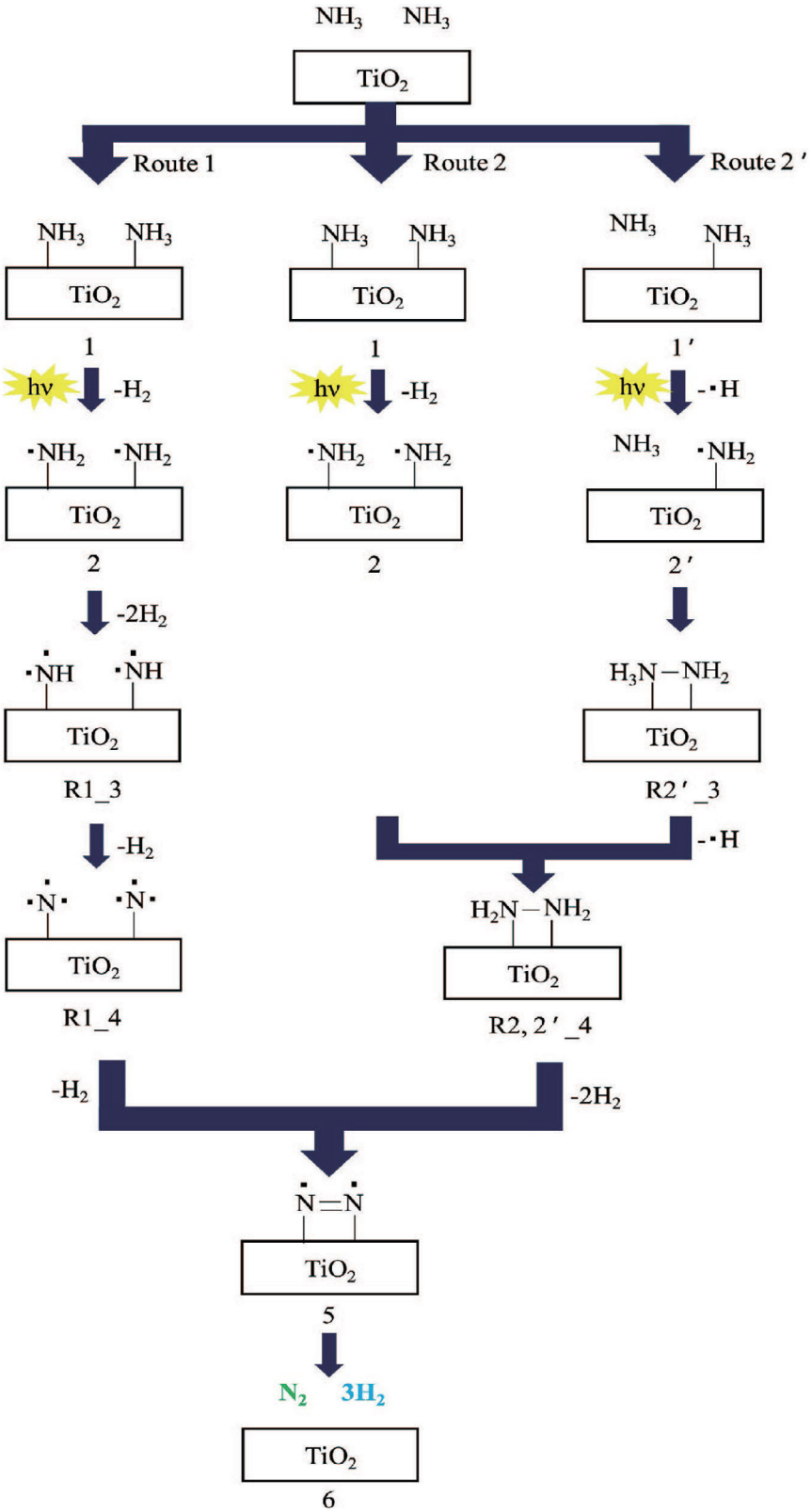

Figure 3. Suggested reaction mechanism for NH_3 decomposition to N_2 and H_2 over TiO_2 photocatalyst, reproduced with permission.[33] Copyright 2017, Elsevier.

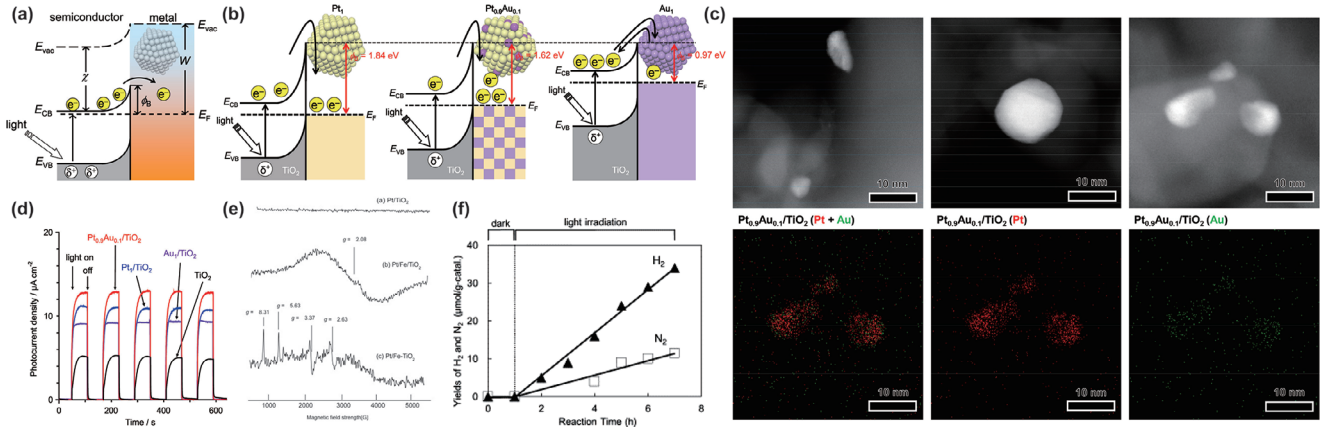

Figure 4. a) Band structure at a metal/semiconductor interface. b) Schematic energy diagrams of Pt_1TiO_2, $Pt_{0.9}Au_{0.1}/TiO_2$, and Au_1/TiO_2 catalysts. c) STEM and EDS mapping of Pt (red) and Au (green) on $Pt_{0.9}Au_{0.1}/TiO_2$. d) Photocurrent responses of different catalysts in NH_3 solution, reproduced with permission.[37] Copyright 2020, ACS. e) ESR spectra of Pt/TiO_2 and Pt/Fe-modified TiO_2. f) Time-dependent H_2 and N_2 yields during NH_3 photodecomposition over Pt/Fe-TiO_2, reproduced with permission.[38] Copyright 2014, Elsevier.

Pt with a lower work function metal can effectively reduce work function (Figure 4b), thereby decreasing φ_B and enhancing electron transfer from TiO_2 to the metal.[50–52]

Shiraishi et al. prepared Pt/TiO_2, Au/TiO_2, and $Pt_{0.9}Au_{0.1}/TiO_2$ catalysts via impregnation, and spherical or hemispherical metal particles were observed on the surface of all three samples (Figure 4c).[37] Photocurrent measurements revealed a higher current density for Pt/TiO_2 than for bare TiO_2 and Au/TiO_2, indicating more efficient transfer of photogenerated conduction band electrons to Pt and ultimately to the FTO substrate. In contrast, the $Pt_{0.9}Au_{0.1}/TiO_2$ sample exhibited an even higher current density than Pt/TiO_2, demonstrating that alloying Pt with 10 mol% Au enhances charge separation (Figure 4d). Consistently, $Pt_{0.9}Au_{0.1}/TiO_2$ also showed the highest hydrogen evolution rate of 285.67 μmol g^{-1} h^{-1} in photocatalytic experiments.

In addition to forming bimetallic alloys, directly doping transition metals into TiO_2 has attracted significant attention. Obata et al. demonstrated that modifying TiO_2 by doping with iron (Fe) before Pt loading can enhance its photocatalytic activity for liquid-phase NH_3 decomposition.[38] This improvement was attributed to substituting Ti^{4+} by Fe^{3+} within the TiO_2 lattice, introducing impurity energy levels, extending light absorption, and improving photon utilization efficiency. This doping effect was confirmed by ESR spectroscopy (Figure 4e). Furthermore, photocatalytic experiments revealed that Fe-doped TiO_2 exhibited a significantly higher stoichiometric hydrogen generation rate than undoped TiO_2 and TiO_2 doped with other transition metals such as Cr (Figure 4f).

2.1.3. Heterojunction Structures

Heterojunction structures have demonstrated significant potential for enhancing photocatalytic performance.[53,54] Inspired by the conventional graphene oxide/titanium dioxide (GO/TiO_2) p–n junction design, Wu et al. developed a nitrogen-doped reduced graphene oxide (rGO)/TiO_2 nanowires (NWs) composite membrane, in which TiO_2 NWs were intercalated throughout the rGO membrane, effectively opening the interlayer spacing and improving membrane permeability (**Figure 5**).[39,55] Notably, spontaneous nitrogen doping occurred in both the rGO sheets and TiO_2 NWs during the photocatalytic reaction in an aqueous ammonia solution. Unlike traditional nitrogen doping techniques that typically require high-energy inputs, such as high-temperature treatments, electrothermal processes, chemical vapor deposition (CVD), plasma treatments, or radiation exposure , the integration of TiO_2 NWs with rGO enabled self-induced nitrogen doping under low-power UV irradiation (8 W, 254 nm).[56–62] Compared with the synthesized pure TiO_2 NWs and commercial P25, the performance was enhanced 30-fold and 14-fold, respectively.

Overall, these three types of TiO_2-based photocatalyst designs illustrate the multidimensional nature of catalyst optimization, progressively addressing critical issues such as enhanced surface area, electron transfer efficiency, radical regulation, and photon utilization efficiency. Future research in this area will necessitate achieving a balance among surface properties, the selection of loaded metals, and precise doping control, while further integrating these factors to maximize photocatalytic performance.

2.2. ZnO-Based Photocatalysts

ZnO is a wide-bandgap semiconductor (bandgap = 3.2 eV; exciton binding energy = 60 meV). Like TiO_2, its photocatalytic efficiency is limited by poor charge separation and rapid carrier recombination. Therefore, further modification is required to enhance its photocatalytic performance. It is well known that the properties of a material are primarily governed by its structure, including morphology, crystal structure, particle size, and surface defects.[63–65] The natural structure of ZnO nanocrystal contains a variety of intrinsic defects, including zinc vacancies (V_{Zn}), oxygen vacancies (V_O), zinc interstitials (Zn_i), oxygen interstitials (O_i), and antisite oxygen defects (O_{Zn}). These features make ZnO a viable platform for photocatalytic NH_3 decomposition when combined with defect engineering and doping.

Reli et al. employed three different synthesis strategies to control and tailor specific defects within the ZnO lattice, particularly

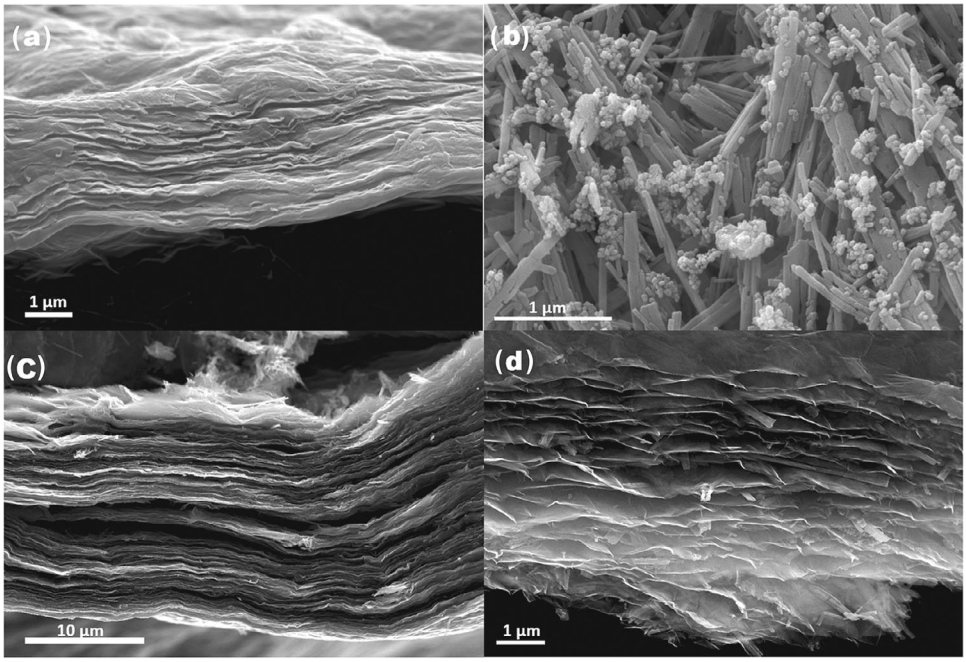

Figure 5. FESEM image of a) rGO membrane, b) TiO_2 NWs, c,d) cross-sectional view of rGO/TiO_2 NWs membrane at different magnifications, reproduced with permission.[39] Copyright 2019, Springer Nature.

oxygen vacancies (V_O) and oxygen interstitials or excess oxygen defects (O_i/O_{Zn}).[29] One ZnO photocatalyst (ZnO(1)) was prepared via thermal annealing of zinc acetate in air (ZnO (1), **Figure 6a**). The other two samples, ZnO (2) and ZnO (3), were synthesized through precipitation of zinc ions using hydroxide ions under different conditions—with and without UV irradiation, respectively (ZnO (3), Figure 6b).

Photoluminescence (PL) spectra of ZnO (1) NPs showed relatively low intensity with a maximum emission around 520 nm (green emission), whereas the ZnO (2) and ZnO (3) samples, synthesized via precipitation, exhibited redshifted emissions peaking near 650 nm (orange-red emission). Furthermore, ZnO (3), which was synthesized under UV irradiation, displayed stronger PL intensity than ZnO (2) (Figure 6c).

It is generally assumed that an increase in surface area should enhance photocatalytic activity, as previously discussed in the context of TiO_2. However, contrary to this expectation, ZnO (1), which exhibited the lowest specific surface area, demonstrated the highest hydrogen evolution rate among the three samples. The green emission in ZnO (1) is attributed to transitions from the CB to deep defect levels associated with oxygen interstitials (O_i or oxygen atoms occupying Zn sites (O_{Zn}). In contrast, the orange-red emission observed in ZnO (2) and ZnO (3) arises from oxygen vacancies (V_O), which introduce very deep donor levels that act as electron traps and hinder photocatalytic activity (Figure 6d).[50] Thus, ZnO (2) and ZnO (3), despite having higher surface areas, suffer from photocatalytic inactivity due to the dominance of V_O defects. In comparison, ZnO (1), obtained via air annealing, favors the formation of excess oxygen defects (O_i/O_{Zn}), as evidenced by its green PL emission, and exhibits superior photocatalytic performance.

2.3. Ruthenium-Based Photocatalysts

Ruthenium-based (Ru-based) catalysts are among the most extensively studied materials for ammonia decomposition and have been widely applied in the thermal decomposition of ammonia experiments. Due to their exceptionally low-temperature activity, Ru-based catalysts have also been explored in photocatalytic applications.[66] The decomposition of NH_3 over Ru-based catalysts has been identified as a structure-sensitive reaction. Specifically, ammonia molecules adsorb on the Ru surface (R1); adsorbed ammonia molecules dissociate and dehydrogenate stepwise (R2, R3, and R4); adsorbed hydrogen atoms recombine to form adsorbed H_2 molecules, which are desorbed as H_2 (R5 and R6); the formation and desorption of N_2 follow the same process as for H_2 (R7 and R8) (**Figure 7a**).[66] The catalytic performance of Ru exhibits a pronounced size effect. Kinoshita et al. suggested that structure-sensitive reactions display particle size-dependent specific reaction rates.[67] On the one hand, an excessively large Ru particle size reduces the number of active sites, leading to a decline in catalytic activity. On the other hand, the Ru atom cluster fails to provide sufficient space for N_2 molecule formation, which requires a minimum of 0.36 nm.

Iwase et al. employed ZnS to support Ru loading and conducted photocatalytic experiments.[40] The bare ZnS photocatalyst produced only H_2 from aqueous ammonia under light irradiation, which was attributed to its relatively high CB potential.[68,69] Even in the absence of any cocatalyst, ZnS was capable of generating H_2 from water containing a sacrificial agent. Moreover, a comparable rate of H_2 evolution was observed when bare ZnS was used in NaOH solution without ammonia, suggesting that hydrogen generation originated primarily from photocorrosion.

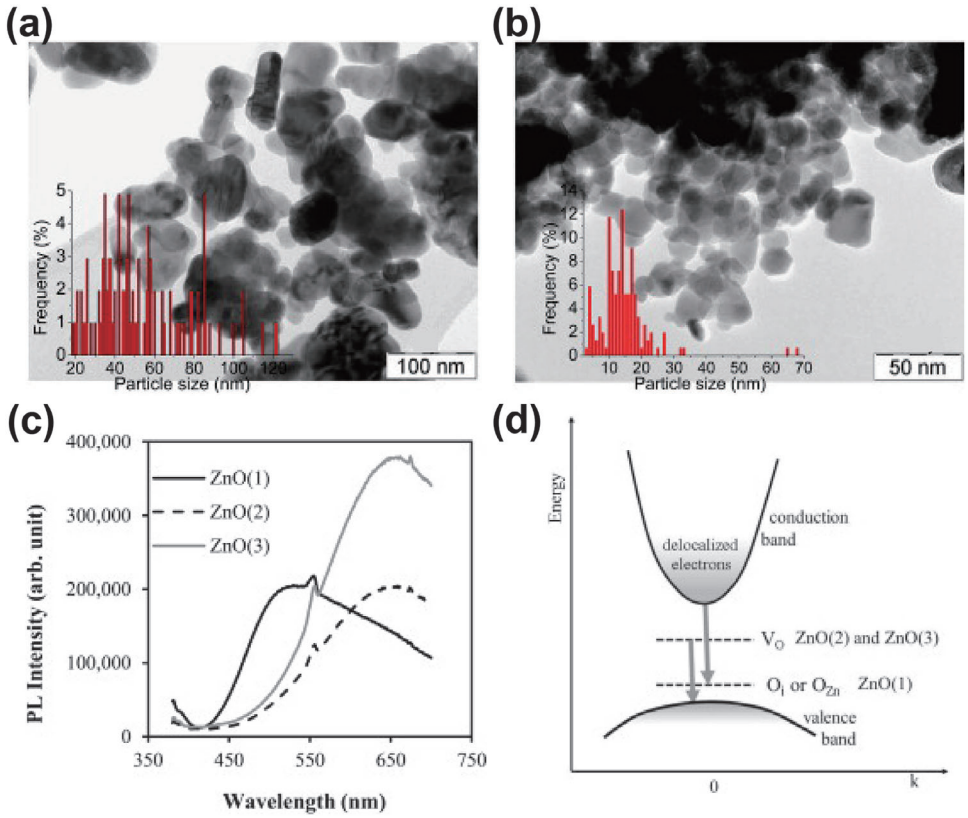

Figure 6. a) TEM image and particle size distribution of ZnO (1) prepared by thermal annealing. b) TEM image of ZnO (3) synthesized by UV-assisted precipitation. c) PL spectra of different ZnO samples. d) Proposed electron transitions corresponding to observed PL peaks, reproduced with permission.[29] Copyright 2015, Elsevier.

In contrast, Ru-loaded ZnS produced stoichiometric amounts of H_2 and N_2 under light irradiation (Ru-loaded ZnS, Figure 7b). The photocatalytic activity reached maximum when the Ru loading was 0.7–1.0 wt%. Notably, the amount of H_2 evolved from Ru/ZnS in aqueous solutions containing a sacrificial agent was significantly lower than that from bare ZnS, indicating that Ru did not function as an active site for water reduction. Instead, it facilitates the oxidation of ammonia to N_2 and simultaneously suppresses the photocorrosion of ZnS. Under simulated solar irradiation, the Ru/ZnS photocatalyst enabled the decomposition of aqueous ammonia into stoichiometric H_2 and N_2 with a turnover number exceeding 1 (Figure 7c). Nevertheless, despite stoichiometric generation, the overall hydrogen yield remained relatively low (5.13 μmol g^{-1} h^{-1}), comparable only to commercial TiO_2. Furthermore, the catalyst exhibited poor stability, as evidenced by a marked decline in performance during the second reaction cycle due to partial Ru detachment and photocorrosion.

In contrast to using Ru solely to suppress substrate photocorrosion, Dzíbelová et al. highlighted the synergistic integration of Ru species with the support material. The study employed a two-dimensional (2D) conductive heme-based substrate capable of effectively anchoring Ru species.[41] HRTEM analysis revealed a lattice fringe spacing of 2.7 Å corresponding to the (104) plane of hematite. In addition, a spacing of 3.2 Å, assigned to the (110) plane of RuO_2, confirmed the successful incorporation of Ru species. Moreover, EDS elemental analysis of the Ru-hematene composite further confirms that Ru oxide NPs were well dispersed across the hematene structure, with no visible agglomeration (Figure 7d,e). This uniform distribution of Ru oxide provides abundant catalytic sites for ammonia oxidation, promoting charge separation and enhancing overall photocatalytic activity.

Upon the incorporation of Ru, the light absorption—particularly in the visible region—was significantly enhanced (Figure 7f). Since the amount of hydrogen generated during photocatalytic reactions does not necessarily scale linearly with the catalyst mass, the optimal catalyst loading was determined based on photocatalytic performance.[70,71] Under optimized conditions (2 mg), the Ru-hematene photocatalyst produced 2.5 times more H_2 than pristine hematene. Furthermore, without any regeneration treatment, Ru-hematene maintained stable photocatalytic performance over five consecutive cycles (120 hours), exhibiting only an 11% decrease in activity (Figure 7g). Rather than serving merely as a protective cocatalyst, Ru in this system forms a strong interfacial interaction with the substrate, enabling a synergistic effect under visible-light irradiation. Specifically, the electronic coupling between Ru and the conductive substrate facilitates the cooperative generation and separation of e^- and h^+, leading to significantly enhanced photocatalytic performance.

However, the photocatalytic performance of this system remains limited by thermodynamic constraints, and its stability is still insufficient for industrial applications. Li et al. designed a photocatalyst composed of gallium nitride NWs vertically aligned

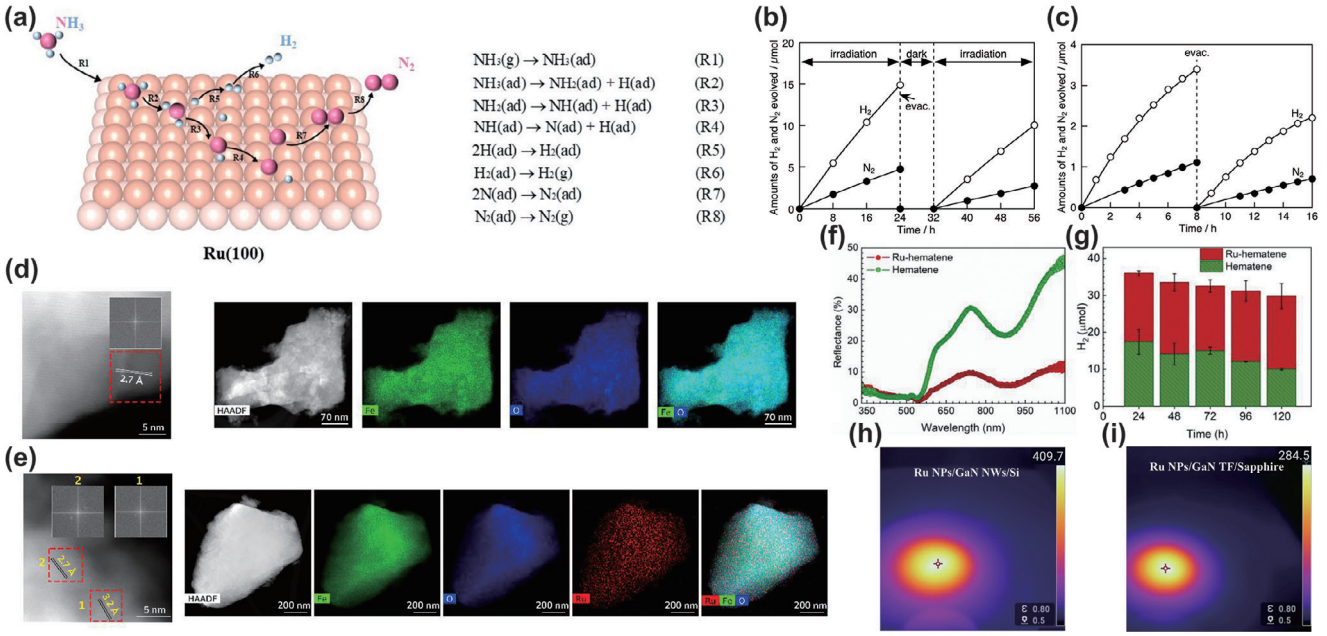

Figure 7. a) Schematic of NH_3 decomposition steps on Ru(100) surface, reproduced with permission.[66] Copyright 2024, Elsevier. b) Time-dependent H_2 and N_2 yields over Ru/ZnS under Xe lamp irradiation. c) NH_3 photodecomposition over ZnS under simulated sunlight (AM 1.5G), reproduced with permission.[40] Copyright 2018, Royal Society of Chemistry. HRTEM, HAADF-STEM, and EDS mapping of d) hematene and e) Ru-hematene. f) UV–vis DRS of hematene and Ru-hematene. g) Recyclability test of hematene and Ru-hematene for NH_3 photodecomposition under visible light, reproduced with permission.[41] Copyright 2023, Elsevier. h,i) Infrared thermal images of Ru NPs/GaN NWs/Si and Ru NPs/GaN TF/Sapphire surface under 5 W·cm^{-2} concentrated light illumination, reproduced with permission.[42] Copyright 2024, Springer Nature.

on a silicon wafer (GaN NWs/Si) to address these challenges. Integrating the silicon substrate introduced a photothermal effect, allowing the surface temperature to reach as high as 409.7 °C under light irradiation at 5 W cm^{-2} without external heating—significantly higher than that of GaN without the Si substrate (Figure 7h,i). This effectively mitigated thermodynamic limitations. In addition, the unique surface properties of the one-dimensional GaN nanostructures enabled long-term catalytic stability for up to 400 hours, demonstrating significant improvements in activity and durability.

3. Photocatalysts for Hydrogen Production from Gas-Phase Ammonia Decomposition

Table 3 summarizes the catalysts reported to date for gas-phase photocatalytic ammonia decomposition to produce hydrogen. Compared with liquid-phase photocatalysis, research in this field has received relatively little attention, and the reported systems are diverse regarding materials design and operating conditions. Overall, the performance of gas-phase reactions is superior to that of liquid-phase reactions, while the specific energy consumption needs to be assessed according to the actual operating conditions. While liquid-phase photocatalysis benefits from simpler reactor setups and controllable reaction environments, it often suffers from limited contact between ammonia molecules and catalyst surfaces, as well as competing redox pathways that generate undesired NO_x byproducts. In contrast, gas-phase systems generally suppress these water-derived side reactions and offer higher selectivity toward H_2 and N_2. Gas-phase photocatalytic ammonia decomposition is governed not only by the intrinsic properties of the catalyst but also by a set of interrelated reaction parameters, including reaction temperature, water vapor content, ammonia partial pressure, gas hourly space velocity (GHSV), and light intensity. For instance, trace amounts of water vapor have been shown to suppress the accumulation of inactive NH_4^+ species on TiO_2 surfaces and promote proton migration to metal sites, thereby sustaining long-term activity.[36] In plasmon-enhanced systems, incident light flux and its associated photothermal effects play a decisive role in generating hot carriers and accelerating surface reactions.[72,73] Meanwhile, GHSV and NH_3 concentration directly influence residence time and surface coverage, determining whether the reaction operates in a transport-limited or surface-kinetic-limited regime. These factors will be highlighted in the discussion of each catalyst category below.

3.1. TiO_2-Based Photocatalysts

TiO_2-based photocatalysts also find application in the gas-phase decomposition of ammonia, and the primary modification method for TiO_2 in this context is metal loading. Hayato Yuzawa and colleagues conducted reactions using a series of M(0.1)/TiO_2 (A) samples to elucidate the role of these loaded metal cocatalysts.[36] Their results showed that each photocatalyst consistently promoted the reaction, producing nearly stoichiometric amounts of N_2 and H_2, with Pt-loaded TiO_2 exhibiting the highest hydrogen production efficiency (**Figure 8a**). Further investigation revealed a near-linear correlation between the work function of the bulk metal and the logarithm of the hydrogen production rate (Figure 8b). Consequently, they concluded

Table 3. Photocatalysts for hydrogen production from gas-phase ammonia decomposition.

Catalyst	Synthesis method	Initial concentration	Catalyst dosage	Light source	Temperature	H_2 production rate [μmol g^{-1} h^{-1}]	Stability	Refs.
Pt(0.1 wt%)/TiO_2	Photodeposition	Airgas, flowing mixture of ammonia gas (1 mL min^{-1}) and Ar (20 mL min^{-1}). Water vapor (25 μmol min^{-1})	600 mg	300 W Xe lamp	323 K	650	/	[36]
Rh(0.1 wt%)/TiO_2	Photodeposition	Airgas, flowing mixture of ammonia gas	600 mg	300 W Xe lamp	323 K	260	/	[36]
Pd(0.1 wt%)/TiO_2	Photodeposition	Airgas, flowing mixture of ammonia gas	600 mg	300 W Xe lamp	323 K	150	/	[36]
Au(0.1 wt%)/TiO_2	Photodeposition	Airgas, flowing mixture of ammonia gas	600 mg	300 W Xe lamp	323 K	110	/	[36]
Ni(0.1 wt%)/TiO_2	Photodeposition	Airgas, flowing mixture of ammonia gas	600 mg	300 W Xe lamp	323 K	50	/	[36]
Cu(0.1 wt%)/TiO_2	Photodeposition	Airgas, flowing mixture of ammonia gas	600 mg	300 W Xe lamp	323 K	20	/	[36]
Cu-Ru-AR	Coprecipitation	Airgas, anhydrous purity, 99.99%	1.5 mg	Supercontinuum laser	300 K	4.32×10^6 (1200 μmol g^{-1} s^{-1})	/	[72]
Cu-Fe-AR	Coprecipitation	Airgas, anhydrous purity, 99.99%	3.7 g	Supercontinuum laser	300 K	1.01×10^5 (18 g d^{-1})	67 h	[73]
SA Ni/CeO_2	Sol–gel process	Airgas, 33%NH_3 / 67%Ar	20 mg	1 Sun	583 K	94 800	72 h	[74]
SA Ni(1.4 wt%)-MCN	Nebulization-coating	Airgas, 5% NH_3/95% Ar	4–6 mg	300 W xenon-arc lamp	325 K	35.6	36 h	[25]
Co@C	Pyrolysis	Airgas, flowing mixture of ammonia gas	30 mg	300 W Xe lamp	523 K	5.03×10^5		[75]
Fe@C	Pyrolysis	Airgas, flowing mixture of ammonia gas	30 mg	300 W Xe lamp	523 K	3.26×10^5		[76]

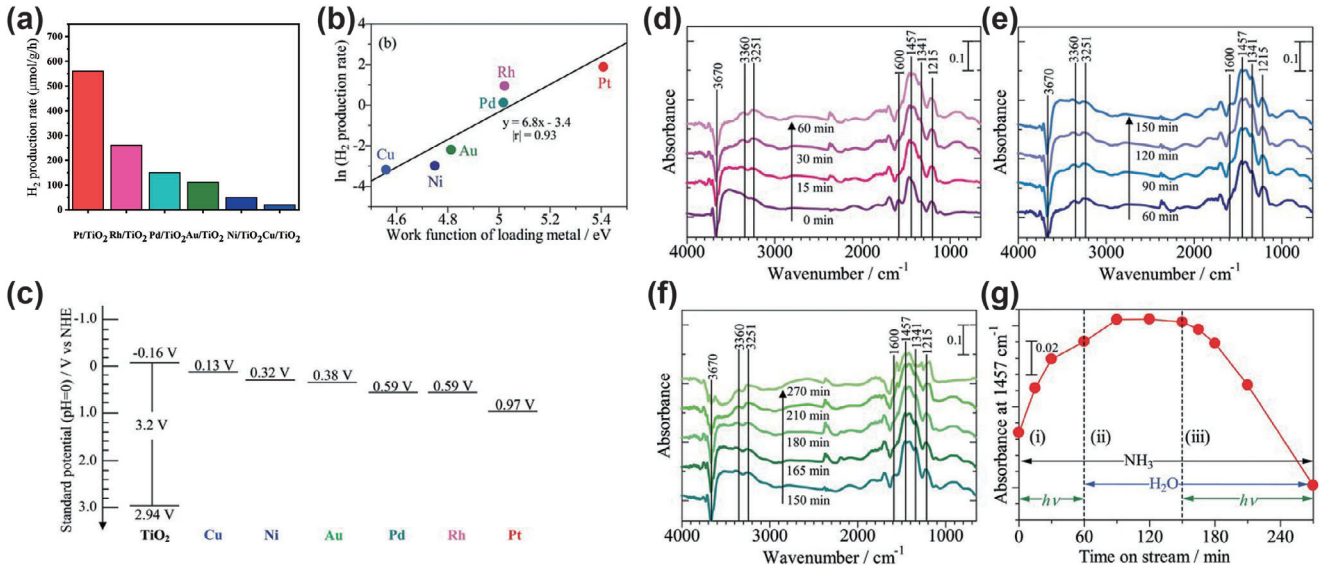

Figure 8. a) H_2 evolution rates over TiO_2 loaded with various transition metals. b) Correlation between H_2 production rate and metal work function. c) Band edge positions of TiO_2 and Fermi levels of loading metals. In situ FTIR spectra of Pt/TiO_2 under different conditions: d) UV irradiation without water vapor, e) dark with water vapor, and f) UV irradiation with water vapor. g) Time evolution of absorbance at 1457 cm^{-1} during these processes, reproduced with permission.[36] Copyright 2012, ACS.

that the promotional effect is not rooted in the conventional understanding of enhanced separation of photogenerated electron–hole pairs. Instead, it stems from the intrinsic catalytic properties of the loaded metal for hydrogen production: a higher metal work function lowers the Fermi level, facilitating the acceptance of photoexcited electrons into the CB of TiO_2 (Figure 8c), thereby enhancing the reduction reactions.

In addition, the researchers emphasized the role of water vapor in gas-phase ammonia decomposition. In situ FTIR spectroscopy was conducted under varying light and water vapor conditions to investigate the surface processes during photocatalytic ammonia decomposition. Under dry photoirradiation (0–60 min, Figure 8d), a gradual increase in the absorption band at 1457 cm^{-1}—corresponding to inactive ammonium ions (NH_4^+)—was observed, along with characteristic bands for coordinated NH_3 and hydrazine intermediates. These findings indicate that, in the absence of water, the interaction between protons and NH_3 leads to the accumulation of NH_4^+ species on the catalyst surface, resulting in photocatalyst deactivation.

Upon stopping irradiation and introducing water vapor (60–150 min, Figure 8e), a partial recovery of the broad band at 3600 cm^{-1} was observed, suggesting readsorption of NH_3 and/or H_2O. Although NH_4^+ formation continued, the presence of water shifted the NH_3—H^+ equilibrium, stabilizing the NH_4^+ concentration rather than reducing it.

When photoirradiation resumed in the presence of NH_3 and H_2O (150–270 min, Figure 8f), a marked decrease in all relevant bands, including that at 1457 cm^{-1}, was recorded (Figure 8g). This result demonstrates that photoexcited electrons effectively reduced NH_4^+, regenerating NH_3 and producing hydrogen radicals (•H). At this stage, water did not act as a reactant but as a dynamic medium facilitating the migration of protons and NH_4^+ to pt sites, thereby promoting their reduction.

Building upon these findings, the authors proposed mechanisms for the photocatalytic ammonia decomposition reaction under two different conditions:

Under UV irradiation, TiO_2 generates h^+ and photoexcited electrons. The h^+ migrate through the VB to surface oxygen sites, and electrons migrate through the CB to the Pt NPs sites (ii). The photogenerated h^+ oxidize adsorbed NH_3, yielding amide radicals (•NH_2) and protons (iii), as confirmed by ESR measurements. The amide radicals subsequently form hydrazine (iv). Assisted by water, the protons move from the TiO_2 surface to the Pt NPs sites, which are reduced by the e^- to form H_2 (v).

Hydrazine primarily undergoes photocatalytic decomposition into diazene and hydrogen, and, to a lesser extent, catalytic decomposition to diazene (vi). Diazene either self-decomposes into hydrogen and nitrogen (vii) or disproportionates to nitrogen and hydrazine (viii). When sufficient water vapor is present (**Figure 9a**), this sequence establishes a continuous photocatalytic cycle, as water acts not as a reactant but rather as a dynamic proton-transfer medium that suppresses NH_4^+ accumulation and maintains active site availability. In contrast, under low-humidity conditions (Figure 9b), photogenerated protons are trapped by ammonia to form surface-bound NH_4^+ species, which cannot readily migrate to Pt sites. This accumulation blocks ammonia oxidation on TiO_2 and leads to catalyst deactivation. Therefore, humidity control is a critical operational parameter for TiO_2-based gas-phase photocatalytic ammonia decomposition, directly determining whether the reaction proceeds sustainably or undergoes rapid deactivation.

Notably, this mechanism is similar to the previously reported TiO_2-based pathway in liquid-phase systems (Figure 3), which proceeds via the dehydrogenation of N_2H_4. During ammonia decomposition, NH_x species couple to form N_2H_4, which subsequently undergoes stepwise dehydrogenation to produce H_2. This pathway predominantly occurs in reactions where water is present. In addition, another N—N recombination pathway typically takes place in anhydrous gas-phase systems; this will be discussed in the following section.

3.2. Antenna-Reactor Photocatalysts

The antenna-reactor (AR) structure is a composite system designed to enhance photocatalytic reactions by integrating plasmonic "antenna" NPs with catalytically active "reactor" sites (**Figure 10a**). The core concept involves coupling plasmonic NPs, which function as optical antennas, with catalytically active materials that serve as reactors to facilitate light-driven chemical transformations.[77] The antenna component, typically Au, Ag, or Cu, captures incident light and generates localized surface plasmon resonance (LSPR), producing energetic hot carriers. The reactor component, often Pd, Pt, or Ru, performs the catalytic transformations. Coupling these two components enables the reactor to harness hot carriers and the enhanced local electromagnetic field, leading to substantial activity improvements beyond its intrinsic light absorption capability.[78–81,82]

Zhou et al. synthesized a plasmonic Cu–Ru–AR photocatalyst by co-precipitation (Figure 10b),[72] achieving an NH_3 decomposition rate of 1200 μmol H_2 g^{-1} s^{-1} under 9.6 W cm^{-2} light irradiation without external heating—20-fold higher than pure Cu and 177-fold higher than pure Ru (Figure 10c). The system exhibited excellent cycling stability under intermittent illumination, maintaining activity over five cycles and producing stoichiometric N_2 and H_2 without any unexpected side reactions (Figure 10d). Notably, when NH_3 decomposition was performed in the dark with an externally heated temperature equivalent to that achieved under illumination, the thermal catalytic hydrogen production rate was one to two orders of magnitude lower than the observed photocatalytic rate (Figure 10e). Considering the limited light penetration within the catalyst particles, the adequate photocatalyst volume was significantly smaller than that under thermal conditions. Thus, the dominant mechanism for AR-catalyzed NH_3 decomposition was attributed to plasmon-induced hot carriers rather than simple photothermal effects.[83] Inspired by the studies above and considering the scarcity and high cost of platinum-group metals (PGMs), Yuan et al. explored the substitution of Ru with earth-abundant transition metals to facilitate large-scale industrial applications.[73,84] In conventional thermally driven reactions, Fe exhibits significantly lower catalytic activity for NH_3 decomposition than Ru, primarily due to the strong Fe—N bond, which hinders product desorption.[85] However, on the surface of NPs, plasmon-induced hot carriers can effectively reduce the activation energy barriers for dissociating both Fe—N and Ru—N bonds. As a result, under ultrafast pulsed laser irradiation, although Fe exhibits inferior thermal catalytic activity compared with Ru-AR, the photocatalytic

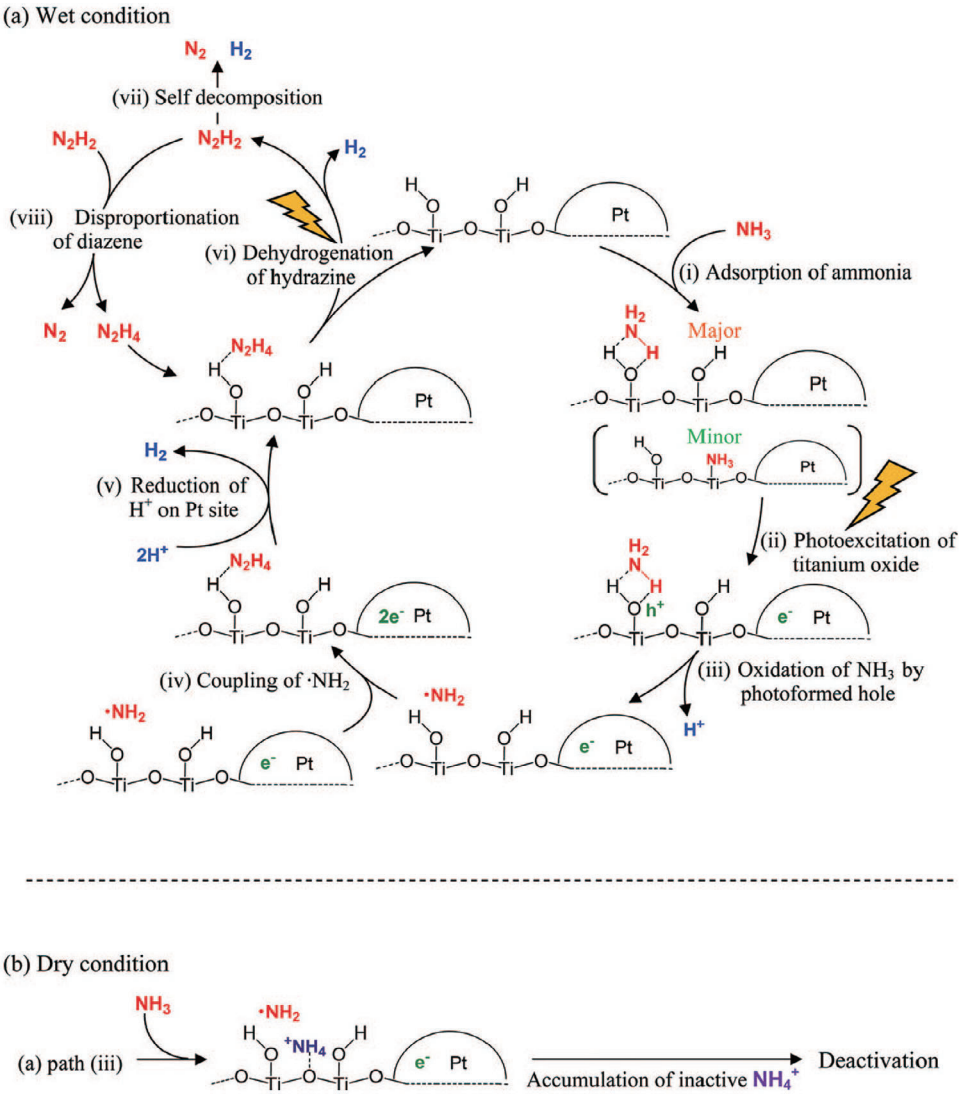

Figure 9. Proposed dominant reaction path of the photocatalytic ammonia decomposition on Pt-loaded titanium oxide a) in the presence of water and b) in the absence of water, reproduced with permission.[36] Copyright 2012, ACS.

performance of Cu–Fe–AR was comparable to that of Cu–Ru–AR (Figure 10f). In gas-phase AR systems, the generation and utilization of plasmon-induced hot carriers are the primary determinants of catalytic activity. These processes are strongly influenced by the incident light conditions—particularly intensity, wavelength alignment with the plasmon resonance peak, and pulse characteristics—which control the number and energy distribution of hot carriers reaching the active sites. Using a high-throughput LED-based photoreactor (Figure 10g), the Cu–Fe–AR catalyst achieved high NH_3 conversion and H_2 production under LED illumination, with an energy efficiency comparable to that observed under laser irradiation. At a power output of 180 W and a feed gas space velocity of 487 h^{-1}, the system attained an NH_3 conversion rate of 72%, corresponding to a daily H_2 yield of 14 g. By comparing the schematic energy diagrams for photocatalysis (excited state) and thermocatalysis (ground state) on Cu–Fe–AR and Cu–Ru–AR (Figure 10h), considering only the two possible rate-determining steps (RDS)—the dissociative adsorption of NH_3 and the associative desorption of N_2—the authors found that the activation energy barriers for both steps on Cu–Fe–AR were significantly reduced upon photoexcitation. This type of mechanism is distinct from the hydrazine-mediated dehydrogenation pathway often observed in water-containing systems and instead represents the other major pathway for ammonia decomposition—the N—N recombination mechanism (Equations (6)–(11))—usually occurring in anhydrous gas-phase conditions, where plasmon-induced hot carriers facilitate bond breaking and formation.

$$NH_3\,(g) + * \rightleftharpoons NH_3* \tag{6}$$

$$NH_3* + * \rightleftharpoons NH_2* + H* \tag{7}$$

$$NH_2* + * \rightleftharpoons NH* + H* \tag{8}$$

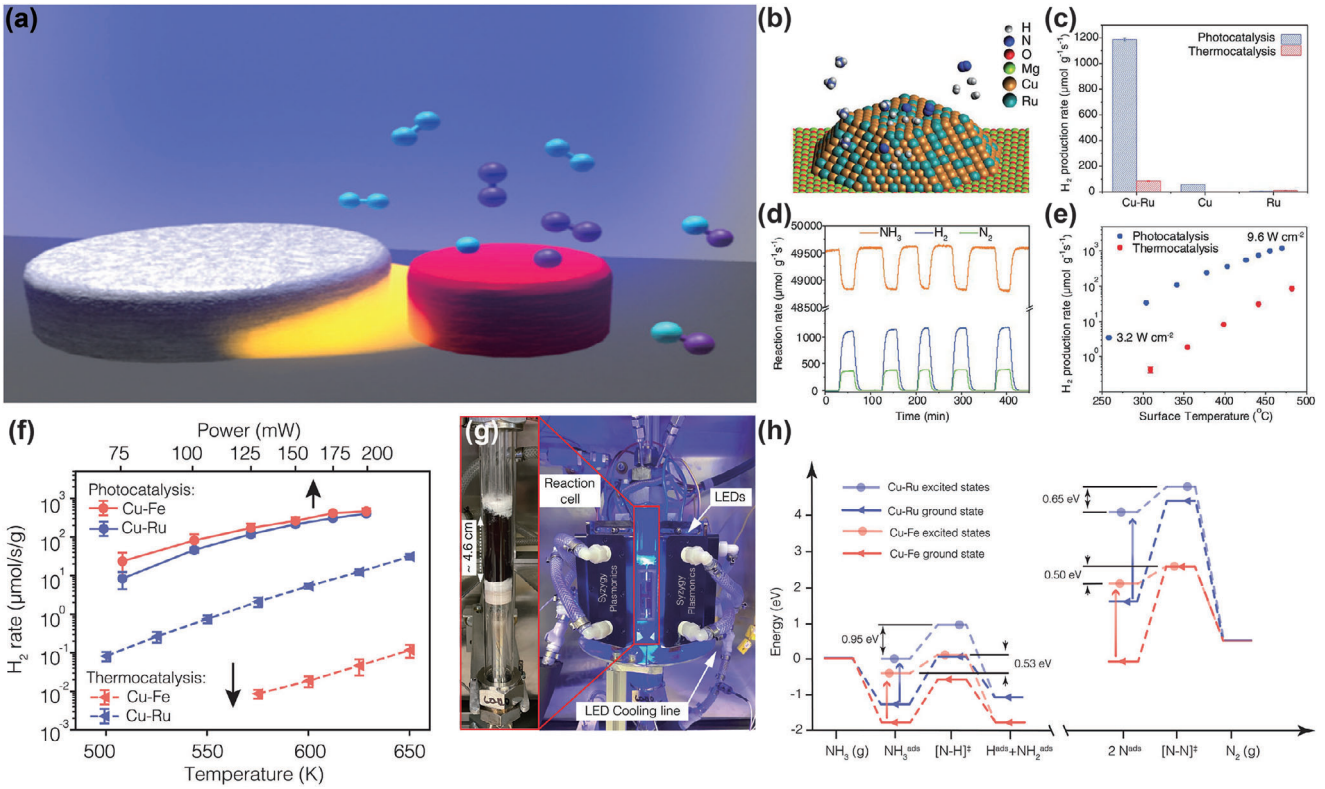

Figure 10. a) Schematic of a plasmonic antenna–catalytic reactor system, reproduced with permission.[77] Copyright 2016, ACS. b) Structural model of Cu-Ru alloy catalyst with Ru as the active site. c) H_2 production rates of Cu-Ru, Cu, and Ru under photo- and thermocatalysis. d) Long-term H_2 evolution on Cu-Ru-AR under light without external heating. e) Comparison of H_2 rates as a function of catalyst surface temperature for photo- and thermocatalysis, reproduced with permission.[72] Copyright 2018, AAAS. f) H_2 production rates over Cu—Fe and Cu—Ru under both catalytic conditions. g) Photograph of the LED-based photocatalytic setup for NH_3 decomposition. h) Energy diagrams comparing reaction pathways under photo- and thermocatalytic conditions for Cu—Fe and Cu—Ru catalysts, reproduced with permission.[73] Copyright 2022, AAAS.

$$NH* + * \rightleftharpoons N* + H* \quad (9)$$

$$2H* \rightleftharpoons H_2(g) \quad (10)$$

$$2N* \rightleftharpoons N_2(g) \quad (11)$$

The combination of earth-abundant materials and cost-effective light sources such as LEDs highlights the potential of AR photocatalysts for sustainable and economically viable hydrogen production from ammonia. Recently, Syzygy Plasmonics, based in Houston, TX, has been advancing the commercialization of this catalytic technology by integrating it with its proprietary light-driven reactor. It has successfully scaled the reaction to achieve hydrogen outputs 500 times higher than laboratory benchmarks, demonstrating its feasibility for pilot-scale deployment.

3.3. Single-Atom Photocatalysts

Since the introduction of the first terminology by Zhang et al. in 2011, single-atom catalysts (SACs) have recently emerged as one of the most innovative and dynamic research frontiers in heterogeneous catalysis.[86–88] Compared to traditional nanoclusters, NPs, and bulk materials, SACs offer several advantages: (i) their unsaturated coordination sites and unique electronic structures confer extremely high activity and selectivity, (ii) the maximum atomic utilization efficiency significantly reduces the use of catalytic metals, (iii) the well-defined single-atom active sites facilitate the identification of reaction mechanisms, and (iv) their atomic-scale structures provide an excellent platform for understanding structure–activity relationships.[89–92]

Li et al. investigated the principles of photocatalytic NH_3 decomposition over Ni single atoms and Ni NPs using DFT (**Figure 11a–c**).[74] Both systems follow the N—N recombination pathway, with the RDS being $N* + 3H* \rightarrow 0.5\ N_2* + 1.5\ H_2$. On Ni (111), this step has a high energy barrier of 1.77 eV, primarily due to nickel nitride's high decomposition energy barrier. In contrast, on the SA Ni/CeO_2 (111) surface, the energy barrier for the same step is only 1.01 eV, and the highest energy barrier for NH_3 dissociation is 1.21 eV, which is 0.56 eV lower than that on Ni (111), indicating that Ni single atoms significantly reduce the reaction energy barrier. In addition, Bader charge analysis showed that the Ni atoms in SA Ni/CeO_2 (111) were positively charged (+1.23 |e|), while those in Ni (111) were nearly neutral (+0.03 |e|), suggesting strong electronic interactions between the Ni single atoms and the CeO_2 support. Specifically, the Ni single atoms lower the energy barrier for ammonia decomposition by transforming the Ni—N bonding mode from covalent to ionic, the latter having a lower bond energy.

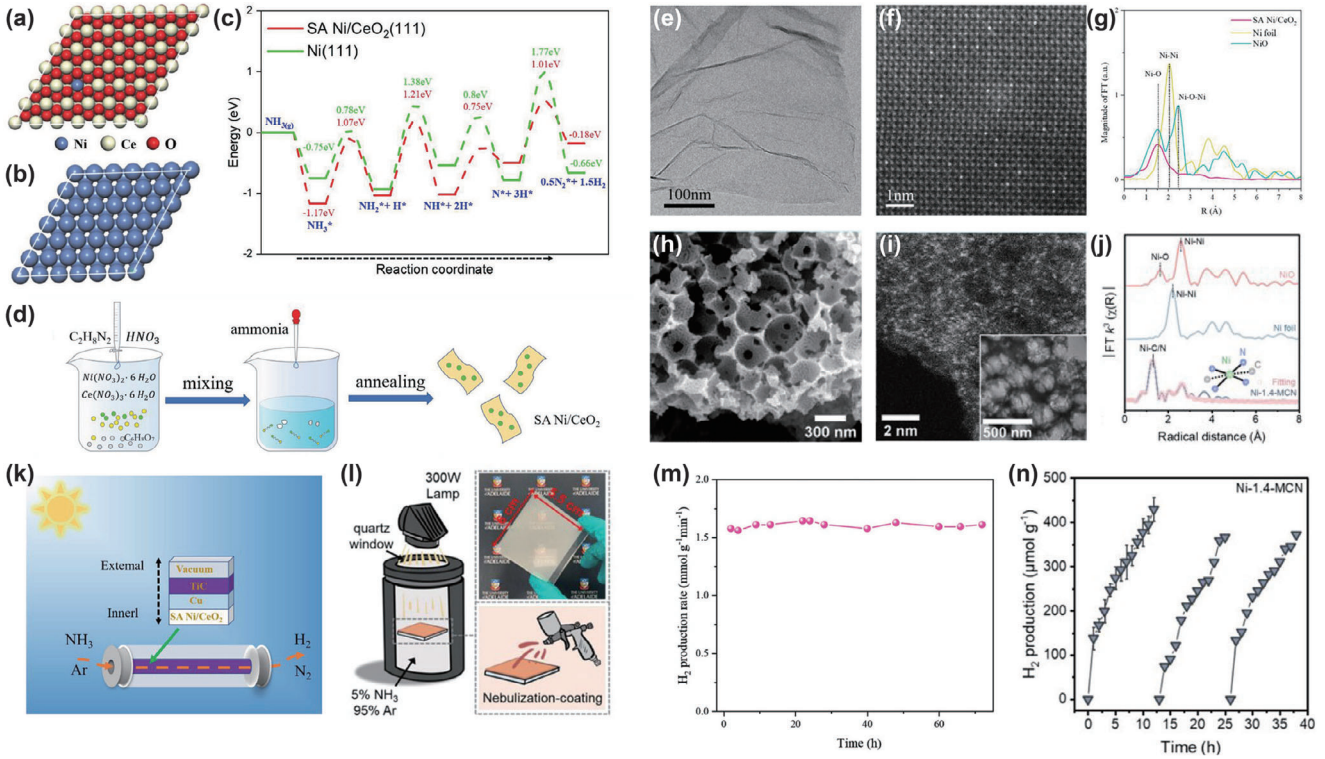

Figure 11. a,b) Atomic models of SA Ni/CeO_2 (111) and Ni (111) surfaces. c) Reaction energy profiles for NH_3 decomposition to H_2 and N_2 on SA Ni/CeO_2 (111) and Ni (111). d) Schematic synthesis process of SA Ni/CeO_2. e,f) TEM and HAADF-STEM images of SA Ni/CeO_2. g) FT-EXAFS spectra at the Ni K-edge, reproduced with permission.[74] Copyright 2022, Wiley. h,i) SEM and AC-HAADF-STEM images of Ni-1.4-MCN. j) FT-EXAFS spectra and fitting curves of Ni foil, NiO, and Ni-1.4-MCN, reproduced with permission.[25] Copyright 2023, ACS. k) Solar-heated NH_3 decomposition system with SA Ni/CeO_2 catalyst, reproduced with permission.[74] Copyright 2022, Wiley. l) Setup illustration and coating process for photocatalyst preparation, reproduced with permission.[25] Copyright 2023, ACS. m) Stability of SA Ni/CeO_2 at 300 °C for 90 h, reproduced with permission.[74] Copyright 2022, Wiley. n) Cycling H_2 production test of Ni-1.4-MCN, reproduced with permission.[25] Copyright 2023, ACS.

According to theoretical calculations, single-atom Ni supported on CeO_2 nanosheets was successfully synthesized via a sol-gel method (Figure 11d). This 2D nanosheet structure (Figure 11e) ensures sufficient contact with reactants during the catalytic process. High-angle annular dark-field scanning transmission electron microscopy (HAADF-STEM) images of SA Ni/CeO_2 reveal several bright spots with diameters of ≈0.1 nm (Figure 11f), indicating the presence of isolated single atoms. X-ray photoelectron spectroscopy (XPS) analysis showed Ni 2p peaks at 854.9 and 872.1 eV, confirming a Ni oxidation state close to +2 (Figure 11g). Experimental results demonstrated that SA Ni/CeO_2 exhibited an ultrahigh hydrogen production rate of 3.544 mmol g^{-1} min^{-1} at 300 °C, outperforming most nonprecious metal catalysts and surpassing certain noble metal catalysts.

Similarly, Lin et al. employed graphitic carbon nitride (C_3N_4), featuring electron-rich "nitrogen pots," as a support to anchor single atoms.[25] Through a one-step silica-templated pyrolysis strategy, they successfully synthesized an ordered macroporous carbon nitride (MCN) with atomically dispersed Ni sites (Figure 11h,i). Fourier-transform extended X-ray absorption fine structure (FT-EXAFS) analysis showed no discernible signals corresponding to Ni—Ni or Ni—O bonds (Figure 11j), confirming the atomic dispersion of Ni species. Experimental results demonstrated that under a low ammonia concentration (5% NH_3/95% Ar), TMs-MCN—particularly Ni-MCN—exhibited a 14-fold increase in hydrogen production compared to pristine MCN.

It is worth noting that both research groups optimized their reaction systems to enhance practical applicability. Li et al. integrated SA Ni/CeO_2 into a custom-designed solar thermal reactor for sunlight-driven NH_3 decomposition. The reactor consisted of a reaction tube coated with a Cu layer, a TiC layer, and a vacuum insulation layer (Figure 11k), enabling nearly complete absorption of sunlight, minimal infrared radiation loss, and weak thermal conduction. As a result, the internal temperature could reach up to 310 °C even under moderate solar intensity (1 sun). In contrast, Lin et al. innovatively fabricated large-scale SAC panels using a facial mist-spray coating method (Figure 11l), an easily scalable and practical approach suitable for industrial-scale device fabrication. Under their customized setups, the systems demonstrated stable hydrogen production over continuous operation for 72 and 36 h, respectively (Figure 11m,n).

3.4. Emerging Catalysts

Metal–organic frameworks (MOFs) have recently emerged as promising candidates for photocatalytic ammonia decomposition, owing to their tunable structures, high surface areas, and diverse active sites.

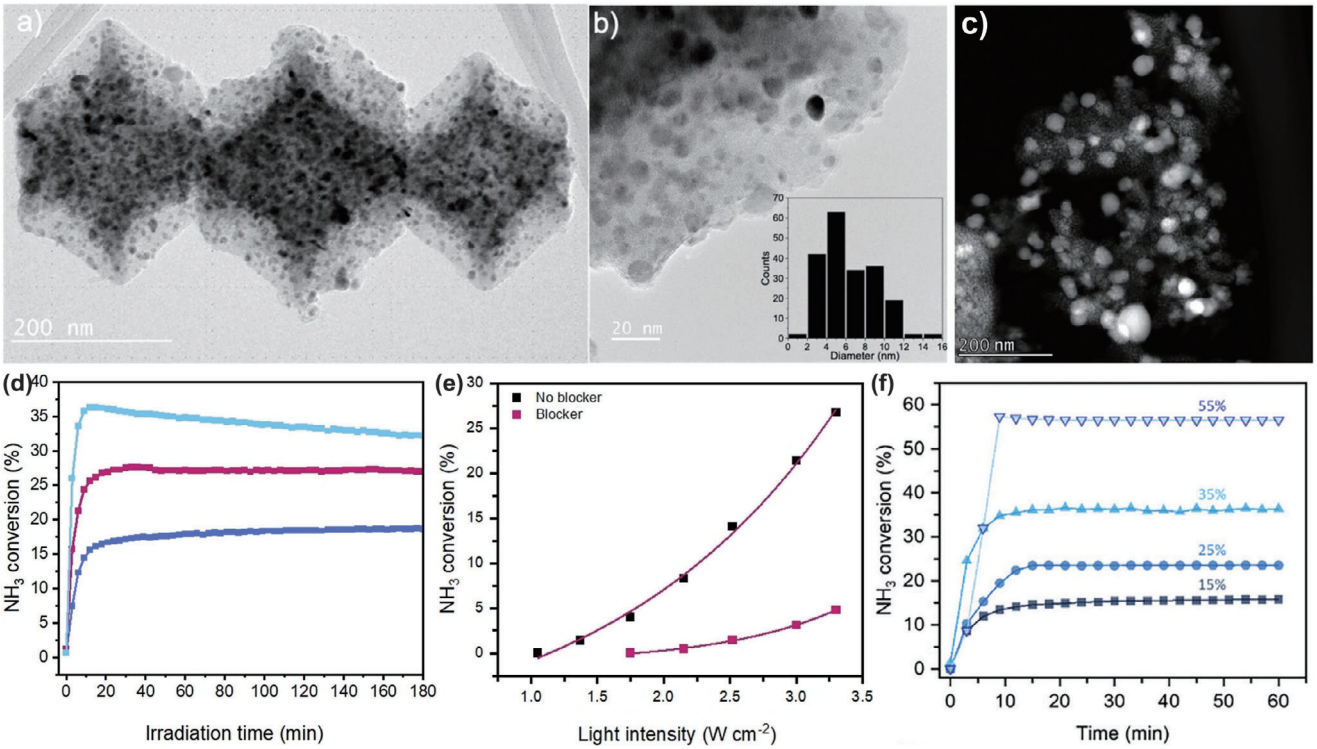

Figure 12. a,b) High-resolution TEM images of Co@C-ZIF-67, reproduced with permission.[75] Copyright 2024, Wiley. c) (HAADF) STEM of Fe@C, reproduced with permission.[76] Copyright 2025, Wiley. d) NH_3 conversion over Co@C–MOFs (ZIF-67 (magenta), ZIF-L (purple), MOF-74 (blue)). e) Co@C–ZIF-67: light-intensity dependence, direct versus indirect illumination (blocker), reproduced with permission.[75] Copyright 2024, Wiley. f) Light-only NH_3 decomposition at varied flow/GHSV (GHSV: 40 000 (black), 20 000 (blue), 10 000 (light blue), and 1000 (gray) mL g^{-1} h^{-1}), reproduced with permission.[76] Copyright 2025, Wiley.

Sousa et al. synthesized three different Co-based catalysts via pyrolysis of parent MOFs, among which Co@C-ZIF-67 exhibited the most promising catalytic performance, maintaining high activity and stability under reaction conditions (**Figure 12**a,b,d).[75] Indirect illumination experiments revealed that at higher light intensities, nonthermal effects contributed more significantly, indicating that although thermal effects were present and partially aided the catalytic activity, the reaction was predominantly driven by pure photochemical effects (Figure 12e). In addition, Sousa et al. further investigated the influence of GHSV on catalytic performance. Using the same pyrolysis approach, Fe@C was prepared and evaluated under various NH_3 GHSV conditions (Figure 12c).[76] At a GHSV of 20 000 mL g^{-1} h^{-1}, the catalyst achieved its highest hydrogen production rate of 326 mmol H_2 g^{-1} h^{-1}, while at a lower GHSV of 1000 mL g^{-1} h^{-1}, a remarkable 55% NH_3 conversion was achieved (Figure 12f).

Most photocatalytic gas-phase ammonia decomposition processes fall within the category of photothermal catalysis. While most reported photothermal catalysts rely on metal NPs supported on metal oxides or semiconductors, there is growing interest in carbon-based supports due to their broad light absorption, high thermal conductivity, and efficient photon-to-heat conversion capability. In this context, materials derived from MOFs also hold great promise as photothermal catalysts, owing to their tunable porosity, composition, and metal–ligand coordination environments. Likewise, 2D materials, despite most of their demonstrated applications being in liquid-phase photocatalysis, possess intrinsic properties—such as high surface-to-volume ratios, tunable electronic structures, and efficient in-plane charge transport—equally advantageous for gas-phase systems. Therefore, exploring MOFs and 2D materials as active platforms for gas-phase ammonia decomposition represents a promising research direction with considerable potential for performance enhancement.

4. Challenges and Future Prospects

As the global transition toward a hydrogen economy accelerates, photocatalytic ammonia decomposition has attracted increasing attention as a sustainable route for carbon-free hydrogen production. However, its practical deployment faces several persistent challenges across thermodynamic, kinetic, material, engineering, and techno-economic dimensions.

4.1. Thermodynamic Constraints and Reactor Design Gaps

Photocatalytic ammonia decomposition is an endothermic reaction that typically proceeds under mild conditions, resulting in inherent thermodynamic limitations. Although extensive efforts have been made to optimize photocatalyst properties, including bandgap modulation, light-harvesting capability, and charge carrier dynamics, comparatively less attention has been given to reactor engineering. In contrast, thermocatalytic systems have seen

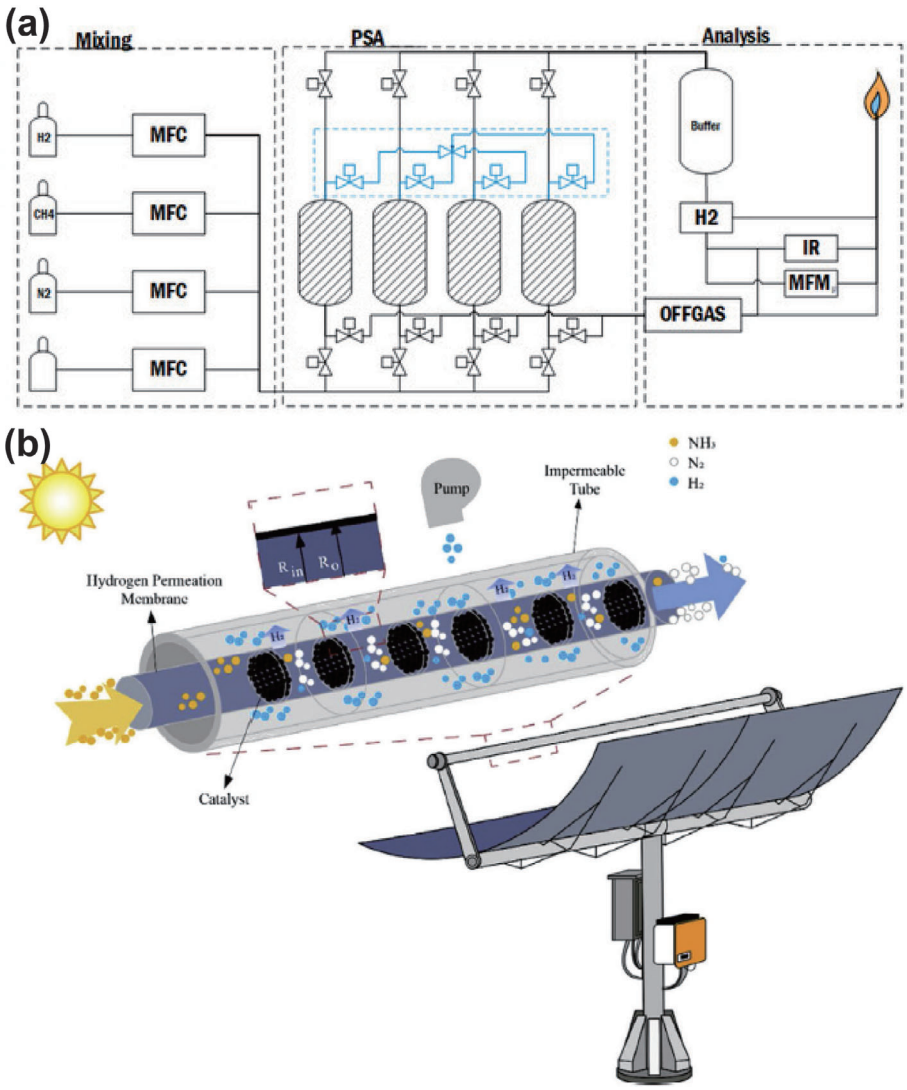

Figure 13. a) Four-bed PSA unit structure, reproduced with permission.[129] Copyright 2022, Elsevier. b) Conceptual diagram of the reactor equipment, reproduced with permission.[130] Copyright 2019, Elsevier.

notable advances in reactor designs that improve energy utilization and facilitate efficient product separation.[93,94] Bridging this gap, recent studies have explored the integration of photocatalysts into tailored photothermal or hybrid reactor systems. For example, customized solar-thermal collector setups have successfully elevated the surface temperature of catalysts without relying on external heating, thereby enhancing the thermodynamic driving force for hydrogen evolution. Furthermore, rational surface engineering, such as developing catalysts with intrinsic photothermal functionalities, has proven effective in improving both reaction kinetics and energy efficiency, while preserving the operational simplicity of photocatalytic systems.

4.2. Kinetic Barriers and Active Site Engineering

Photocatalytic ammonia decomposition is primarily limited by the high bond energy of the N—H bond in ammonia molecules, as well as sluggish surface reaction steps, including NH_3 activation and the subsequent N—N coupling to form N_2. These rate-limiting steps demand innovative catalytic strategies to reduce activation energies. Recent advances, such as SACs,[95] plasmonic enhancement,[96,97] and co-catalyst engineering,[98] have shown great potential for improving surface reaction kinetics. Future directions include the rational design of tailored active sites that stabilize key intermediates, and the harnessing of plasmon-induced hot carriers and/or local electric field to facilitate challenging bond activation steps.[99–102] Coupling these developments with in situ/operando spectroscopies will be critical for validating proposed mechanisms and guiding further design.

4.3. Material Innovation and Cost Considerations

To date, the photocatalytic system remains heavily reliant on TiO_2 materials, which dominate nearly half of the existing studies.

Furthermore, the loaded metals, as the cocatalyst, in these systems are predominantly noble metals such as Pt, Pd, and Ru, which entail high costs and hinder practical implementation. Expanding the material space is essential. Recent years have witnessed growing exploration of alternative materials, including transition metal oxides, transition metal sulfides, lanthanide compounds, and main-group element-based compounds, which have laid the groundwork. Consequently, further developing multimetal or heterostructured systems combining earth-abundant elements could offer synergistic effects while reducing reliance on costly elements, deserving a crucial focus for future research. In parallel, machine learning (ML) has emerged as a transformative data-driven strategy, leveraging computational tools to provide insights and predictions based on trained datasets.[103–112] Thus far, numerous studies have combined ML with ammonia decomposition. He et al. developed an ML-high-throughput DFT framework focused on the N—N recombination mechanism to screen the activity of dual-atom catalysts, successfully predicting the catalytic performance of 2187 candidate structures.[113] Zhao et al. also based their approach on the N—N recombination pathway, applying ML to correlate nitrogen adsorption energies with reaction barriers in different Ni-based alloys, ultimately identifying NiZn and $NiCu_3$ as promising non-noble catalysts.[114] Meanwhile, Guo et al. employed random forest, support vector machine (SVM), and gradient boosting regression models to map ammonia decomposition performance as a function of catalyst properties and reaction conditions, achieving robust predictive accuracy ($R^2 > 0.85$) and revealing temperature and GHSV as critical parameters.[115] ML combined with automated high-throughput experimentation has demonstrated its great potential in accelerating the screening of broad functional materials with different application potentials, including the catalytic materials for energy conversion applications.[116–121] Thus, ML techniques are poised to play a pivotal role in the screening, designing, and optimizing photocatalysts for ammonia decomposition, enabling cost-effective yield enhancement and inspiring innovative research directions. By leveraging large datasets and predictive modeling, ML can significantly shorten the development cycle for efficient and affordable photocatalysts, particularly when integrated with automation in experimental workflows.

4.4. Stability and Scalability

Although the hydrogen production performance of photocatalytic ammonia decomposition has steadily improved in recent years, it still lags significantly behind that of well-established thermal decomposition processes. There remains considerable room for advancement. Currently, most stability evaluations of photocatalysts are limited to short-term laboratory testing (typically less than 100 h), which falls far short of the rigorous standards required for industrial hydrogen production. During prolonged operation, common deactivation issues include surface site blocking/poisoning, support photocorrosion, and active species migration or aggregation. Surface poisoning typically occurs in TiO_2-based systems, where the accumulation of reaction intermediates such as NH_X and N_2H_X species tends to hinder sustained activity. In gas-phase systems, the introduction of water vapor is often employed as a transfer medium to remove these intermediates, while in liquid-phase systems, lowering the ammonia concentration can suppress their buildup. Unlike relatively photostable TiO_2, some semiconductors, such as metal sulfides, are prone to photocorrosion under high light flux. Typical countermeasures include constructing heterojunctions, heteroatom doping, and protective shielding strategies.[122–124] For migration or aggregation of active species, stabilization can be achieved by employing strongly anchoring supports or dispersing the active phase within porous carbon frameworks—a strategy particularly relevant under elevated temperature conditions and in single-atom catalyst systems.[75,76] By tailoring stabilization strategies to specific deactivation mechanisms and application scenarios, catalyst lifetime can be extended while maintaining activity. These advances are essential for bridging the gap between short-term laboratory demonstrations and the long-term stability requirements of practical hydrogen production. Long-term pilot testing under realistic conditions is also urgently needed to validate scalability and durability.

4.5. System-Level Integration, Industrial Relevance, and Life Cycle Assessment

Photocatalytic ammonia decomposition technologies are often studied in isolation, with few studies addressing their implementation in industrial-scale ammonia cracking systems. Critical aspects such as upstream and downstream process integration, strategies for handling and purifying the produced hydrogen, and its alignment with broader hydrogen value chains remain largely unexplored.

As the second most produced chemical commodity worldwide, ammonia benefits from a mature storage and transportation infrastructure, primarily via high-pressure storage at ambient temperature (1.5–1.8 MPa) or cryogenic storage at atmospheric pressure.[125,126] Owing to its corrosivity toward copper, silver, and related alloys, ammonia-compatible materials must be employed in equipment fabrication. To mitigate issues such as uneven photothermal distribution and low surface-to-volume ratios, current ammonia decomposition systems are developed mainly at small to medium scales.[127] ML has also been applied to reactor optimization. For example, Pourali et al. combined computational fluid dynamics (CFD), artificial neural networks (ANN), and response surface methodology (RSM) to identify how design variables affect ammonia conversion, efficiency, and H_2 flow, and proposed optimized reactor prototypes.[128] These insights are also highly relevant for guiding future photocatalytic reactor design, offering a data-driven pathway to improve system efficiency and scalability.

Hydrogen generated from ammonia decomposition requires purification strategies aligned with end-use requirements. Pressure swing adsorption (PSA) remains the most prevalent method, offering operational simplicity and hydrogen purities exceeding 99.99%. It makes it indispensable for applications such as proton exchange membrane fuel cells (PEMFCs) that demand ultra-high purity.[131] Kalman et al. developed a four-bed PSA unit with a 12-step adsorption–desorption cycle, achieving hydrogen concentrations as high as 99.95% (**Figure 13a**).[129] Membrane separation is another viable approach. Wang et al. proposed a model that couples a solar concentrator with a catalytic Pd–Ag

membrane reactor, achieving nearly complete ammonia conversion (99%) at 200 °C and 0.1 bar (Figure 13b).[130] While high-temperature systems often use noble-metal alloy membranes for their thermal stability, the lower operating temperatures of photocatalytic systems permit the use of cost-effective polymer or inorganic membranes.

In some applications, ultra-high hydrogen purity is not required. For example, alkaline fuel cells (AFCs) can tolerate up to 9% ammonia in the hydrogen stream, while high-temperature PEMFCs withstand even higher concentrations, easing the stringency of purification demands.[94,132] Considering economic costs, a PSA–membrane hybrid system can be adopted, offering greater cost savings than conventional PSA alone. In addition, the unreacted ammonia recovery system is crucial since PSA units may suffer from ammonia poisoning during long-term operation.

Future research should focus on coupling these systems with renewable ammonia synthesis processes (e.g., electrochemical nitrogen reduction) and developing complete off-grid hydrogen production units. Moreover, comprehensive life cycle assessments (LCAs) and techno-economic analyses (TEAs) are needed. Concretely, LCAs should specify clear system boundaries and a functional unit (e.g., 1 kg H_2 at 99.9% purity), include inventories for catalyst synthesis and replacement, reactor fabrication, electricity for light sources or auxiliaries, ammonia feed production route (green vs conventional), and downstream purification, then report impact metrics with uncertainty ranges. For TEA, a transparent cost model should be provided that breaks down Capital Expenditure (CAPEX) and Operating Expenditure (OPEX), considering optical efficiency and illuminated area, wall-plug efficiency for LEDs (if applicable), to evaluate energy input, emissions, and cost relative to established methods like steam methane reforming or thermal ammonia cracking.[133] These studies will help identify scenarios where photocatalytic decomposition offers competitive advantages.

4.6. Policy, Regulatory, and Deployment Considerations

In parallel with technical advances, attention should be given to regulatory frameworks, safety guidelines, and economic incentives for photocatalytic hydrogen production. The alignment of research objectives with government hydrogen strategies and green ammonia infrastructure will play a pivotal role in accelerating commercialization. Pilot demonstrations supported by policy incentives or public–private partnerships can facilitate the translation of lab-scale advances to real-world applications.

5. Conclusion

This review has presented a comprehensive analysis of recent progress in photocatalytic ammonia decomposition as a sustainable pathway for hydrogen production. Emphasis was placed on categorizing photocatalysts by their reaction phase (gas phase and liquid phase), and systematically evaluating conventional semiconductors, especially TiO_2 and ZnO, emerging single-atom catalysts, architectural enhancements, and advanced hybrid systems. Phase-dependent reaction mechanisms and performance optimization strategies were also critically discussed to illuminate the underlying principles governing catalytic behavior.

Despite notable advances in material design and mechanistic understanding, the diversity of photocatalysts remains limited, and key challenges persist across multiple fronts, including thermodynamic constraints, sluggish kinetics, catalyst instability, and insufficient system-level integration. The emerging application of data-driven techniques, such as ML and automated high-throughput experimentation, offers promising avenues to accelerate materials discovery and optimization.

Moving forward, greater emphasis must be placed on interdisciplinary innovation—bridging materials science, reactor engineering, computational modeling, and systems analysis—to achieve practical, scalable, and cost-effective solutions. Integrating photocatalytic ammonia decomposition into broader hydrogen energy systems, supported by robust techno-economic and life cycle assessments, will be essential to realizing its potential in the global transition toward clean energy.

We hope this review serves as both a timely reference and an inspiration for future research aimed at overcoming existing limitations and unlocking the full potential of photocatalytic ammonia decomposition in the emerging hydrogen economy.

Acknowledgements

Z.Y. and X.J. contributed equally to this work. The authors acknowledge the financial support from the Australian Research Council (FT230100059, DP240100687, and IH220100012).

Open access publishing facilitated by Australian National University, as part of the Wiley - Australian National University agreement via the Council of Australian University Librarians.

Conflict of Interest

The authors declare no conflict of interest.

Keywords

catalyst design, hydrogen production, machine learning, photocatalytic ammonia decomposition, solar energy

Received: June 19, 2025
Revised: August 28, 2025
Published online: September 26, 2025

[1] C. Le Quéré, G. P. Peters, P. Friedlingstein, R. M. Andrew, J. G. Canadell, S. J. Davis, R. B. Jackson, M. W. Jones, *Nat. Clim. Change* **2021**, *11*, 197.
[2] M. K. Hubbert, *Science* **1949**, *109*, 103.
[3] H. D. Matthews, S. Wynes, *Science* **2022**, *376*, 1404.
[4] M. Kaltschmitt, W. Streicher, A. Wiese, *Renewable Energy: Technology, Economics and Environment*, Springer Science & Business Media, New York **2007**.
[5] T. Covert, M. Greenstone, C. R. Knittel, *J. Econ. Perspect.* **2016**, *30*, 117.
[6] F. P. Martins, S. D.-L. Almaraz, A. B. B. Junior, C. Azzaro-Pantel, P. Parikh, *Renewable Sustainable Energy Rev.* **2024**, *204*, 114796.
[7] Z. Abdin, *Renewable Sustainable Energy Rev.* **2024**, *200*, 114572.
[8] Y.-L. Hsieh, S.-C. Yeh, *Discover Sustainability* **2024**,*5*, 31.
[9] H. W. Kamran, M. Rafiq, A. Abudaqa, A. Amin, *Environ. Technol.* **2024**, *45*, 3439.

[10] J. O. M. Bockris, *Int. J. Hydrogen Energy* **2013**, *38*, 2579.
[11] P. P. Edwards, V. L. Kuznetsov, W. I. H. David, *Philos. Trans. R. Soc., A* **2007**, *365*, 1043.
[12] S. P. Filippov, A. B. Yaroslavtsev, *Russ. Chem. Rev.* **2021**, *90*, 627.
[13] C. M. White, R. R. Steeper, A. E. Lutz, *Int. J. Hydrogen Energy* **2006**, *31*, 1292.
[14] J. O. Abe, A. Popoola, E. Ajenifuja, O. M. Popoola, *Int. J. Hydrogen Energy* **2019**, *44*, 15072.
[15] A. Kovač, M. Paranos, D. Marciuš, *Int. J. Hydrogen Energy* **2021**, *46*, 10016.
[16] D. Mori, K. Hirose, *Int. J. Hydrogen Energy* **2009**, *34*, 4569.
[17] M. Aziz, *Energies* **2021**, *14*, 5917.
[18] S. Sherif, N. Zeytinoglu, T. Veziroğlu, *Int. J. Hydrogen Energy* **1997**, *22*, 683.
[19] A. Boretti, *Chem. Eng. Res. Des.* **2025**, *217*, 235.
[20] A. Boisen, S. Dahl, J. K. Nørskov, C. H. Christensen, *J. Catal.* **2005**, *230*, 309.
[21] T. He, P. Pachfule, H. Wu, Q. Xu, P. Chen, *Nat. Rev. Mater.* **2016**, *1*, 16059.
[22] X. Zhang, Y. Zhao, X. Jia, Y. Zhao, L. Shang, Q. Wang, G. I. Waterhouse, L. Z. Wu, C. H. Tung, T. Zhang, *Adv. Energy Mater.* **2018**, *8*, 1702780.
[23] Y. Zhao, Y. Zhao, G. I. Waterhouse, L. Zheng, X. Cao, F. Teng, L. Z. Wu, C. H. Tung, D. O'Hare, T. Zhang, *Adv. Mater.* **2017**, *29*, 1703828.
[24] E. P. Perman, G. A. S. Atkinson, W. Ramsay, *Proc. R. Soc. London* **1905**, *74*, 110.
[25] J. Lin, Y. Wang, W. Tian, H. Zhang, H. Sun, S. Wang, *ACS Catal.* **2023**, *13*, 11711.
[26] N. Kannan, D. Vakeesan, *Renewable Sustainable Energy Rev.* **2016**, *62*, 1092.
[27] A. J. Nozik, *Annu. Rev. Phys. Chem.* **1978**, *29*, 189.
[28] J. Ji, X. Duan, G. Qian, X. Zhou, G. Tong, W. Yuan, *Int. J. Hydrogen Energy* **2014**, *39*, 12490.
[29] M. Reli, M. Edelmannová, M. Sihor, P. Praus, L. Svoboda, K. K. Mamulová, H. Otoupalíková, L. Capek, A. Hospodková, L. Obalová, K. Koc, *Int. J. Hydrogen Energy* **2015**, *40*, 8530.
[30] H. Wang, Y. Su, H. Zhao, H. Yu, S. Chen, Y. Zhang, X. Quan, *Environ. Sci. Technol.* **2014**, *48*, 11984.
[31] S. Zhang, Z. He, X. Li, J. Zhang, Q. Zang, S. Wang, *Nanoscale Adv.* **2020**, *2*, 3610.
[32] H. Kominami, H. Nishimune, Y. Ohta, Y. Arakawa, T. Inaba, *Appl. Catal., B* **2012**, *111*, 297.
[33] A. Utsunomiya, A. Okemoto, Y. Nishino, K. Kitagawa, H. Kobayashi, K. Taniya, Y. Ichihashi, S. Nishiyama, *Appl. Catal., B* **2017**, *206*, 378.
[34] S. Abdul Razak, A. H. Mahadi, R. Thotagamuge, D. Prasetyoko, H. Bahruji, *Catal. Lett.* **2023**, *153*, 1013.
[35] M. Reli, N. Ambrožová, M. Šihor, L. Matějová, L. Čapek, L. Obalová, Z. Matěj, A. Kotarba, K. Kočí, *Appl. Catal., B* **2015**, *178*, 108.
[36] H. Yuzawa, T. Mori, H. Itoh, H. Yoshida, *J. Phys. Chem. C* **2012**, *116*, 4126.
[37] Y. Shiraishi, S. Toi, S. Ichikawa, T. Hirai, *ACS Appl. Nano Mater.* **2020**, *3*, 1612.
[38] K. Obata, K. Kishishita, A. Okemoto, K. Taniya, Y. Ichihashi, S. Nishiyama, *Appl. Catal., B* **2014**, *160*, 200.
[39] Z. Wu, N. Ambrožová, E. Eftekhari, N. Aravindakshan, W. Wang, Q. Wang, S. Zhang, K. Kočí, Q. Li, *Emergent Mater.* **2019**, *2*, 303.
[40] A. Iwase, K. Ii, A. Kudo, *Chem. Commun.* **2018**, *54*, 6117.
[41] J. Dzíbelová, S. M. H. Hejazi, V. Šedajová, D. Panáček, P. Jakubec, Z. Baďura, O. Malina, J. Kašlík, J. Filip, Š. Kment, M. Otyepka, R. Zbořil, *Appl. Mater. Today* **2023**, *34*, 101881.
[42] J. Li, B. Sheng, Y. Chen, J. Yang, P. Wang, Y. Li, T. Yu, H. Pan, L. Qiu, Y. Li, J. Song, L. Zhu, X. Wang, Z. Huang, B. Zhou, *Nat. Commun.* **2024**, *15*, 7393.
[43] A. L. Linsebigler, G. Lu, J. T. Yates, *Chem. Rev.* **1995**, *95*, 735.
[44] X. Chen, S. S. Mao, *Chem. Rev.* **2007**, *107*, 2891.
[45] H. Hussain, G. Tocci, T. Woolcot, X. Torrelles, C. L. Pang, D. S. Humphrey, C. M. Yim, D. C. Grinter, G. Cabailh, O. Bikondoa, R. Lindsay, J. Zegenhagen, A. Michaelides, G. Thornton, *Nat. Mater.* **2017**, *16*, 461.
[46] J. Tao, T. Luttrell, M. Batzill, *Nat. Chem.* **2011**, *3*, 296.
[47] A. Naldoni, M. Allieta, S. Santangelo, M. Marelli, F. Fabbri, S. Cappelli, C. L. Bianchi, R. Psaro, D. Santo, *J. Am. Chem. Soc.* **2012**, *134*, 7600.
[48] Y. Nakato, K. Ueda, H. Yano, H. Tsubomura, *J. Phys. Chem.* **1988**, *92*, 2316.
[49] D. E. Eastman, *Phys. Rev. B* **1970**, *2*, 1.
[50] Y. Shiraishi, H. Sakamoto, Y. Sugano, S. Ichikawa, T. Hirai, *ACS Nano* **2013**, *7*, 9287.
[51] I. Pašti, S. Mentus, *Mater. Chem. Phys.* **2009**, *116*, 94.
[52] R. Ishii, K. Matsumura, A. Sakai, T. Sakata, *Appl. Surf. Sci.* **2001**, *169*, 658.
[53] S. Cheng, Z. Sun, K. H. Lim, A. A. Wibowo, T. Zhang, T. Du, L. Liu, H. T. Nguyen, G. K. Li, Z. Yin, S. Kawi, *ACS Catal.* **2023**, *13*, 7221.
[54] S. Cheng, Z. Sun, K. H. Lim, K. Liu, A. A. Wibowo, T. Du, L. Liu, H. T. Nguyen, G. K. Li, Z. Yin, S. Kawi, *Appl. Catal., B* **2024**, *343*, 123583.
[55] W. Wang, Z. Wu, E. Eftekhari, Z. Huo, X. Li, M. O. Tade, C. Yan, Z. Yan, C. Li, Q. Li, D. Zhao, *Catal. Sci. Technol.* **2018**, *8*, 1704.
[56] Y. Cong, J. Zhang, F. Chen, M. Anpo, *J. Phys. Chem. C* **2007**, *111*, 6976.
[57] R. Nakamura, T. Tanaka, Y. Nakato, *J. Phys. Chem. B* **2004**, *108*, 10617.
[58] J. Wang, D. N. Tafen, J. P. Lewis, Z. Hong, A. Manivannan, M. Zhi, M. Li, N. Wu, *J. Am. Chem. Soc.* **2009**, *131*, 12290.
[59] O. Diwald, T. L. Thompson, T. Zubkov, S. D. Walck, J. T. Yates, *J. Phys. Chem. B* **2004**, *108*, 6004.
[60] Y.-C. Lin, C.-Y. Lin, P.-W. Chiu, *Appl. Phys. Lett.* **2010**, *96*, 133110.
[61] X. Wang, X. Li, L. Zhang, Y. Yoon, P. K. Weber, H. Wang, J. Guo, H. Dai, *Science* **2009**, *324*, 768.
[62] D. Wei, Y. Liu, Y. Wang, H. Zhang, L. Huang, G. Yu, *Nano Lett.* **2009**, *9*, 1752.
[63] D. Chen, Z. Wang, T. Ren, H. Ding, W. Yao, R. Zong, Y. Zhu, *J. Phys. Chem. C* **2014**, *118*, 15300.
[64] N. M. Flores, U. Pal, R. Galeazzi, A. Sandoval, *RSC Adv.* **2014**, *4*, 41099.
[65] K. N. Abbas, N. Bidin, *Appl. Surf. Sci.* **2017**, *394*, 498.
[66] Z. Su, J. Guan, Y. Liu, D. Shi, Q. Wu, K. Chen, Y. Zhang, H. Li, *Int. J. Hydrogen Energy* **2024**, *51*, 1019.
[67] K. Kinoshita, *J. Electrochem. Soc.* **1990**, *137*, 845.
[68] S. Yanagida, T. Azuma, H. Sakurai, *Chem. Lett.* **2006**, *11*, 1069.
[69] J. F. Reber, K. Meier, *J. Phys. Chem.* **1984**, *88*, 5903.
[70] S. Cao, L. Piao, *Angew. Chem., Int. Ed.* **2020**, *59*, 18312.
[71] M. Qureshi, K. Takanabe, *Chem. Mater.* **2017**, *29*, 158.
[72] L. Zhou, D. F. Swearer, C. Zhang, H. Robatjazi, H. Zhao, L. Henderson, L. Dong, P. Christopher, E. A. Carter, P. Nordlander, N. J. Halas, *Science* **2018**, *362*, 69.
[73] Y. Yuan, L. Zhou, H. Robatjazi, J. L. Bao, J. Zhou, A. Bayles, L. Yuan, M. Lou, M. Lou, S. Khatiwada, E. A. Carter, P. Nordlander, N. J. Halas, *Science* **2022**, *378*, 889.
[74] Y. Li, Q. Guan, G. Huang, D. Yuan, F. Xie, K. Li, Z. Zhang, X. San, J. Ye, *Adv. Energy Mater.* **2022**, *12*, 2202459.
[75] A. Sousa, A. Rendon Patino, L. Garzon Tovar, D. Mateo, J. Gascon, A. Bavykina, *ChemSusChem* **2025**, *18*, 202401896.
[76] A. Sousa, D. Mateo, L. Garzon-Tovar, K. Brennan, A. Rendón-Patiño, N. Morlanés, X. Wang, J. C. Navarro, J. Ruiz-Martinez, M. García-Melchor, *Small* **2025**, *21*, 2411468.
[77] C. Zhang, H. Zhao, L. Zhou, A. E. Schlather, L. Dong, M. J. McClain, D. F. Swearer, P. Nordlander, N. J. Halas, *Nano Lett.* **2016**, *16*, 6677.

[78] V. Giannini, A. I. Fernández-Domínguez, S. C. Heck, S. A. Maier, *Chem. Rev.* **2011**, *111*, 3888.
[79] G. V. Hartland, *Chem. Rev.* **2011**, *111*, 3858.
[80] J. S. DuChene, W. Niu, J. M. Abendroth, Q. Sun, W. Zhao, F. Huo, W. D. Wei, *Chem. Mater.* **2013**, *25*, 1392.
[81] X. Liu, X. Jing, R. Liu, P. Guo, Z. Yin, *Energy Fuels* **2024**, *38*, 4966.
[82] Y. Zhang, S. He, W. Guo, Y. Hu, J. Huang, J. R. Mulcahy, W. D. Wei, *Chem. Rev.* **2018**, *118*, 2927.
[83] H. Robatjazi, H. Zhao, D. F. Swearer, N. J. Hogan, L. Zhou, A. Alabastri, M. J. McClain, P. Nordlander, N. J. Halas, *Nat. Commun.* **2017**, *8*, 27.
[84] S. Zhang, X. He, Y. Ding, Z. Shi, B. Wu, *Renewable Sustainable Energy Rev.* **2024**, *204*, 114821.
[85] G. Ertl, M. Huber, *J. Catal.* **1980**, *61*, 537.
[86] B. Qiao, A. Wang, X. Yang, L. F. Allard, Z. Jiang, Y. Cui, J. Liu, J. Li, T. Zhang, *Nat. Chem.* **2011**, *3*, 634.
[87] C. Zhu, S. Fu, Q. Shi, D. Du, Y. Lin, *Angew. Chem., Int. Ed.* **2017**, *56*, 13944.
[88] H. Zhang, G. Liu, L. Shi, J. Ye, *Adv. Energy Mater.* **2018**, *8*, 1701343.
[89] C. Gao, J. Low, R. Long, T. Kong, J. Zhu, Y. Xiong, *Chem. Rev.* **2020**, *120*, 12175.
[90] Y. Wang, J. Mao, X. Meng, L. Yu, D. Deng, X. Bao, *Chem. Rev.* **2019**, *119*, 1806.
[91] X. Li, X. Yang, Y. Huang, T. Zhang, B. Liu, *Adv. Mater.* **2019**, *31*, 1902031.
[92] A. Wang, J. Li, T. Zhang, *Nat. Rev. Chem.* **2018**, *2*, 65.
[93] N. Li, C. Zhang, D. Li, W. Jiang, F. Zhou, *Chem. Eng. J.* **2024**, *495*, 153125.
[94] S. Chiuta, R. C. Everson, H. W. Neomagus, P. Van der Gryp, D. G. Bessarabov, *Int. J. Hydrogen Energy* **2013**, *38*, 14968.
[95] Y. He, Y. Zhang, G. Hao, W. Jiang, J. Di, *Nanoscale* **2024**, *16*, 22077.
[96] C. Bhattacharya, S. E. Saji, A. Mohan, V. Madav, G. Jia, Z. Yin, *Adv. Energy Mater.* **2020**, *10*, 2002402.
[97] W. Wang, S. E. Saji, S. Karutur, H. Zheng, G. Meng, Y. Cheng, Z. Yin, *Chem. Res. Chin. Univ.* **2020**, *36*, 1000.
[98] H. Lu, J. Tournet, K. Dastafkan, Y. Liu, Y. H. Ng, S. K. Karuturi, C. Zhao, Z. Yin, *Chem. Rev.* **2021**, *121*, 10271.
[99] Z. Sun, S. Cheng, X. Jing, K. Liu, Y.-L. Chen, A. A. Wibowo, H. Yin, M. Usman, D. MacDonald, S. Cheong, R. F. Webster, L. Gloag, N. Cox, R. D. Tilley, Z. Yin, *Adv. Mater.* **2024**, *36*, 2406088.
[100] S. Cheng, Z. Sun, K. H. Lim, C. Li, M. Judd, N. Cox, R. Hocking, Y. Liu, X. Jing, X. Liao, G. Jia, S. Kawi, Z. Yin, *Nano Energy* **2025**, *139*, 110917.
[101] N. Uddin, Z. Sun, J. Langley, H. Lu, P. Cao, A. Wibowo, X. Yin, C. S. Tang, H. T. Nguyen, J. D. Evans, X. Li, X. Zhang, M. Heggen, R. E. Dunin-Borkowski, A. T. S. Wee, H. Zhao, N. Cox, Z. Yin, *Proc. Natl. Acad. Sci. USA* **2023**, *120*, 2212075120.
[102] Z. Sun, S. Cheng, R. Luo, X. Jing, H. Yin, K. Liu, A. A. Wibowo, K. H. Lim, H. T. Nguyen, N. Cox, *ACS Catal.* **2025**, *15*, 2250.
[103] Z. Wang, Z. Sun, H. Yin, X. Liu, J. Wang, H. Zhao, C. H. Pang, T. Wu, S. Li, Z. Yin, X. F. Yu, *Adv. Mater.* **2022**, *34*, 2104113.
[104] Q. Tao, P. Xu, M. Li, W. Lu, *npj Comput. Mater.* **2021**, *7*, 23.
[105] H. Yin, Z. Sun, Z. Wang, D. Tang, C. H. Pang, X. Yu, A. S. Barnard, H. Zhao, Z. Yin, *Cell Rep. Phys. Sci.* **2021**, *2*, 100482.
[106] F. Lai, Z. Sun, S. E. Saji, Y. He, X. Yu, H. Zhao, H. Guo, Z. Yin, *Small* **2021**, *17*, 2100024.
[107] M. Zhong, K. Tran, Y. Min, C. Wang, Z. Wang, C.-T. Dinh, P. De Luna, Z. Yu, A. S. Rasouli, P. Brodersen, S. Sun, O. Voznyy, C.-S. Tan, M. Askerka, F. Che, M. Liu, A. Seifitokaldani, Y. Pang, S.-C. Lo, A. Ip, Z. Ulissi, E. H. Sargent, *Nature* **2020**, *581*, 178.
[108] A. Jaison, A. Mohan, Y.-C. Lee, *Mater. Sci. Eng., R* **2024**, *161*, 100880.
[109] S. Tunala, S. Zhai, F. Wu, Y.-H. Chen, *Sci. China: Chem.* **2025**, *68*, 3415.
[110] K. Li, H. Du, L. Liu, H. Yang, J. Fang, D. Li, *J. Ind. Eng. Chem.* **2025**, *151*, 146.
[111] J. Bhattacharjee, S. Roy, A. A. Shaikh, *Energy* **2025**, *360*, 100027.
[112] J. Liu, L. Liang, B. Su, D. Wu, Y. Zhang, J. Wu, C. Fu, *J. Mater. Inf.* **2024**, *4*, 33.
[113] G. He, H. Yan, R. Fan, M. Zhao, J. Liu, Y. Zhou, Z. Zou, Z. Li, *Small Methods* **2025**, 2500023.
[114] S. Zhao, H. Feng, P. Pu, Y. Deng, Z. Ge, X. Song, T. Liu, Y. Yang, M. Wei, X. Zhang, *Int. J. Hydrogen Energy* **2025**, *150*, 150051.
[115] W. Guo, A. Shafizadeh, H. Shahbeik, S. Rafiee, S. Motamedi, S. A. G. Nia, M. H. Nadian, F. Li, J. Pan, M. Tabatabaei, *J. Energy Storage* **2024**, *89*, 111688.
[116] S. Cheng, Z. Sun, K. H. Lim, T. Z. H. Gani, T. Zhang, Y. Wang, H. Yin, K. Liu, H. Guo, T. Du, L. Liu, G. K. Li, Z. Yin, S. Kawi, *Adv. Energy Mater.* **2022**, *12*, 2270079.
[117] A. Chen, X. Zhang, Z. Zhou, *InfoMat* **2020**, *2*, 553.
[118] Z. Sun, H. Yin, K. Liu, S. Cheng, G. K. Li, S. Kawi, H. Zhao, G. Jia, Z. Yin, *SmartMat* **2022**, *3*, 68.
[119] Z. Sun, H. Yin, Z. Yin, *Matter* **2023**, *6*, 2553.
[120] H. Zhao, W. Chen, H. Huang, Z. Sun, Z. Chen, L. Wu, B. Zhang, F. Lai, Z. Wang, M. L. Adam, C. H. Pang, P. K. Chu, Y. Lu, T. Wu, J. Jiang, Z. Yin, X. F. Yu, *Nat. Synth.* **2023**, *2*, 505.
[121] B. Burger, P. M. Maffettone, V. V. Gusev, C. M. Aitchison, Y. Bai, X. Wang, X. Li, B. M. Alston, B. Li, R. Clowes, N. Rankin, B. Harris, R. S. Sprick, A. I. Cooper, *Nature* **2020**, *583*, 237.
[122] Y. P. Xie, Z. B. Yu, G. Liu, X. L. Ma, H. Cheng, *Energy Environ. Sci.* **2014**, *7*, 1895.
[123] H. Huang, B. Dai, W. Wang, C. Lu, J. Kou, Y. Ni, L. Wang, Z. Xu, *Nano Lett.* **2017**, *17*, 3803.
[124] Y. Tang, X. Hu, C. Liu, *Phys. Chem. Chem. Phys.* **2014**, *16*, 25321.
[125] M. Aravindan, V. Madhan Kumar, V. S. Hariharan, T. Narahari, P. Arun Kumar, K. Madhesh, G. Praveen Kumar, R. Prabakaran, *Renewable Sustainable Energy Rev.* **2023**, *188*, 113791.
[126] J. D. Hunt, B. Zakeri, A. Nascimento, M. A. V. de Freitas, F. d. C. Amorim, F. Guo, G.-J. Witkamp, B. van Ruijven, Y. Wada, *Int. J. Hydrogen Energy* **2024**, *53*, 875.
[127] R. Chen, R. Wang, X. Lu, S. Zhao, Y. Liao, H. Pan, Z. Zhan, H. Tang, *J. Ind. Eng. Chem.* **2024**, *134*, 1.
[128] M. Pourali, J. A. Esfahani, H. Jahangir, A. Farzaneh, K. C. Kim, *J. Energy Storage* **2022**, *55*, 105804.
[129] V. Kalman, J. Voigt, C. Jordan, M. Harasek, *Sustainability* **2022**, *14*, 14037.
[130] B. Wang, H. Kong, H. Wang, Y. Wang, X. Hu, *Int. J. Hydrogen Energy* **2019**, *44*, 26874.
[131] D. Mao, J. M. Griffin, R. Dawson, A. Fairhurst, N. Bimbo, *Int. J. Hydrogen Energy* **2021**, *46*, 23380.
[132] T. Hejze, J. O. Besenhard, K. Kordesch, M. Cifrain, R. R. Aronsson, *J. Power Sources* **2008**, *176*, 490.
[133] X. Jing, F. Li, Y. Wang, *Catal. Sci. Technol.* **2022**, *12*, 2912.

Zhuohao Yang is currently a Master's degree student at the Research School of Chemistry, Australian National University (Australia). He got his B.S. from Shandong University (China) and Australia National University (Australia) in 2024. He is now focusing on the ammonia decomposition to produce hydrogen through photocatalysis.

Xuechen Jing is currently a Ph.D. student at the Research School of Chemistry, The Australian National University. He received his M. Eng. degree from the University of Sydney and B.S. degree from Northeast Petroleum University. His research focuses on single-atom catalysis and the development of functional nanomaterials for energy conversion applications.

Zongyou Yin obtained his B.S. and M.S. degrees at Jilin University in China, and completed his Ph.D. at Nanyang Technological University (NTU) in Singapore. Then, he started his postdoc careers at NTU/Singapore, IMRE/Singapore, followed by MIT and then Harvard University. Dr Yin started his own Research Group at Australian National Univesrity (ANU) from 2017. His group's research is interdisciplinary, encompassing AI-driven materials innovations, nano-to-atomic materials science, fundamental relationship among materials-structures-devices, and synergistic integration of multifunctions towards systems for energy and wearable applications.